Mineralogy, fluid inclusions, and S–Pb isotope geochemistry study of the Tuboh Pb–Zn–Ag polymetallic deposit, Lubuklinggau, Sumatra, Indonesia

Jinhong Xu[a,b], Zhengwei Zhang[a,*], Chengquan Wu[a,*], Qiao Shu[a], Chaofei Zheng[a,b], Xiyao Li[a,b], Ziru Jin[a,b]

[a] State Key Laboratory of Ore Deposit Geochemistry, Institute of Geochemistry, Chinese Academy of Sciences, Guiyang 550081, China
[b] University of Chinese Academy of Sciences, Beijing 100049, China

ABSTRACT

The Tuboh Pb–Zn–Ag polymetallic deposit is located in Lubuklinggau, Sumatra, Indonesia. The ore bodies occur within the contact zone between the Eocene Jangkat quartz monzonite and limestone of the Jurassic–lower Cretaceous Rawas Formation and are controlled by skarn and NE–SW faults. In order to reveal the relationship between mineralization and magmatism, a comprehensive study was conducted that included detailed field observation, petrographic study, fluid inclusions, and S–Pb isotope analysis. The results include the following findings. 1) Four mineralization stages were recognized. The prograde stage is characterized by garnet and wollastonite. The retrograde stage is dominated by magnetite, hematite, chlorite, quartz, with minor sulfides. The quartz-sulfide stage is enriched in sphalerite, galena, chalcopyrite, pyrite, pyrrhotite and quartz. The quartz–calcite stage is typified by quartz and calcite. 2) Electron probe microanalysis (EPMA) results revealed that garnet in the Tuboh deposit is rich in andradite ($Adr_{37\text{-}99}Grs_{1\text{-}59}$), indicating skarn was formed under relatively oxidized conditions. The temperature and S fugacity for sphalerite crystallization were 270 to 392 °C, and $10^{-9.7}$ to $10^{-7.1}$ bars, respectively. The decreasing trend between S fugacity with temperature suggests that ore precipitation occurred in a progressive reducing environment. EPMA analyses demonstrate that the Ag is primarily hosted by galena, which is present as solid solution with Bi via coupled substitution of Pb in the galena. 3) Fluid inclusions trapped in garnet indicates that the ore-forming fluid was high in temperature with high to moderate salinity, at 380–450 °C, 9.21–21.4 wt% NaCl equivalent, respectively, which indicates ore-forming fluid may derive from magmatic fluids. Fluid inclusions from quartz suggest ore precipitation from cooler and moderate- to low-salinity fluids, at 337–420 °C and 6.45–11.1 wt% NaCl equivalent, respectively, which is in agreement with the sphalerite crystallization temperature. The fluid inclusions in the quartz and calcite reveal that ore-forming fluid from the post-ore stage was moderate to low in both temperature and salinity, at 151–266 °C and 0.35–7.45 wt% NaCl equivalent, respectively. The positive correlation between homogenization temperature and salinity indicates that the ore-forming fluid mixed with meteoric water. 4) The $\delta^{34}S$ values of sulfides range from −2.44 to 2.52‰, suggesting a magmatic origin of S. The Pb isotopic ratios of the galena are very uniform and have low radiogenic Pb, at $^{206}Pb/^{204}Pb$ = 18.342–18.370, $^{207}Pb/^{204}Pb$ = 15.576–15.599, and $^{208}Pb/^{204}Pb$ = 38.369–38.430. This indicates that the metals originated from the Eocene Jangkat quartz monzonite. Finally, in combination of available data suggest that the Tuboh deposit is a typical skarn-type Pb–Zn–Ag polymetallic deposit, which is the result of the Eocene quartz monzonite intruded the Jurassic–Cretaceous Rawas Formation, and ore precipitation is the consequent of the mixture of ore-forming fluid with meteoric water and decreases in S fugacity.

1. Introduction

Numerous Sn–W, Cu–Au, and Ag–Pb–Zn deposits occur in Sumatra, Indonesia (Fig. 1), including skarn, porphyry, epithermal, and sediment-hosted deposits. Previous studies mainly focused on hydrothermal Sn–W mineralization related to granites (Clake and Beddoe-stephens, 1987; Darbyshire, 1988; Schwartz and Surjono, 1990a, b; Schwartz and Surjono, 1991; Ng et al., 2017), porphyry Cu–Au deposits (van Leeuwen et al.,1987; Susanto and Suparka, 2012; Maryono et al., 2014), and epithermal Au–Ag deposits (Jobson et al., 1994; van Leeuwen et al.,
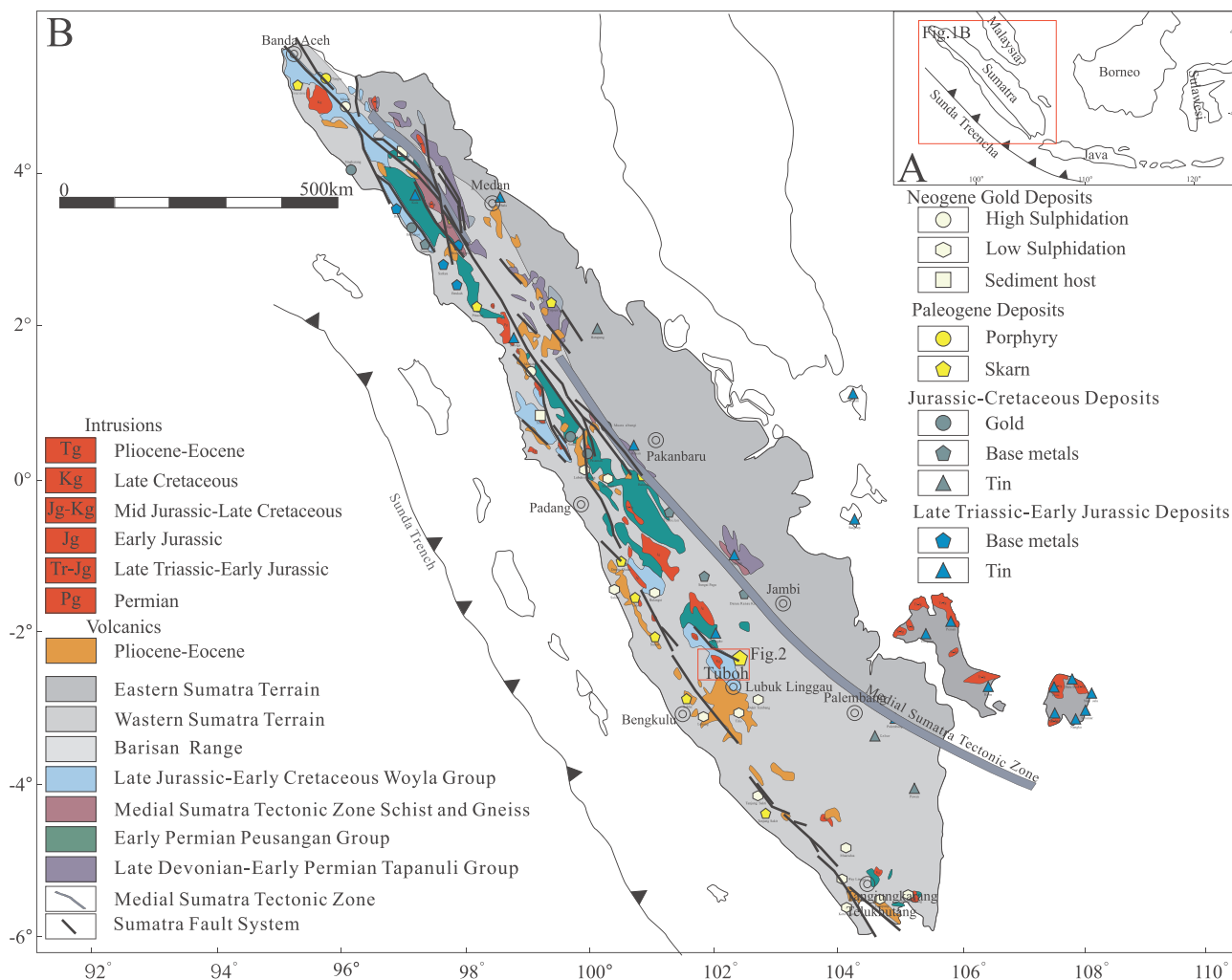
Fig. 1. A. Tectonic sketch map of Sumatra. B. Geological map and distributions of metal deposits in Sumatra (modified from Barber and Crow, 2005).

1987; Williamson and Fleming, 1995; Wheeler et al., 2001; Barber and Crow 2003; Garwin et al., 2005; Sutopo, 2011; Saing et al., 2015). However, skarn deposits are also widespread in this region (Fig. 1), including the Muara Sipongi skarn Au (Beddoe-Stephens et al., 1987), Tangse skarn Cu–Mo (van Leeuwen et al., 1987), the skarn Cu (Imtihanah, 2000; Hu et al., 2014), and Nam Salu skarn Sn (Schwartz and Surjono, 1990b) deposits.

The Tuboh Pb–Zn–Ag polymetallic deposit is located in Jangkat District, Musi Rawas Regency, Lubuklinggau, South Sumatra, Indonesia (Fig. 2; JICA, 1988; Abidin, 2010; Abidin and Utoyo, 2014). The Japan International Cooperation Agency (JICA) conducted a detailed geologic mapping and mineral survey (JICA, 1986). In addition, drillings by the PT Galtam Co. revealed that the Zn–Pb–Cu–Ag mineralization has a genetic relationship with marble and hornfels (Prayogo, 2009). Moreover, the Centre for Geological Survey (CGS; Bandung, Indonesia) considered that the Arai Granite resulted in the formation of skarn alteration zones (Abidin, 2010). We discovered some skarn alteration zones and mineralization points of Au, Cu, Fe, and Zn–Pb in and around the Tuboh deposit. This deposit is one of the better-investigated skarns in this region. However, the process of mineralization, sources of metallogenic materials, and nature of the ore-forming fluids have not been well studied. In this paper, we describe the geological characteristics of the Tuboh deposit in detail and discuss the characteristics of the ore-forming fluid and the evolution of the ore-forming environment through research based on mineralogy, fluid inclusions, and isotope geochemistry. Finally, we analyze the relationship between the

formation stage of the skarn and the ore-forming process.

2. Geological settings

Sumatra is located in the west of Sunda Arc and has a complex tectonic evolution that commenced in the late Paleozoic, continued to the Cenozoic, and includes multiple phase of subduction, collision, accretion, and uplift (Katili, 1973; Hamilton, 1979; McCourt et al., 1996; Barber and Crow, 2005; Metcalfe, 2006). The tectonic framework of Sumatra consists of East Sumatra Terrain, West Sumatra Terrain, and Woyla Nappe (Fig. 1), which was assembled at different times (Hall, 1996, 2002; Metcalfe, 1996, 2006).

The East Sumatra Terrain is represented by the Late Devonian–early Permian Tapanuli Group (Cameron et al. 1980; Pulunggono and Cameron 1984) and has similarities with the Sibumasu Block (Şengör, 1984; Metcalfe, 2011). The West Sumatra Terrain contains the Permo–Triassic Peusangan Group and has natural affinity with the Cathaysian Block (Hutchison, 1994; Barber and Crow, 2003). This terrain was accreted toward the East Sumatra terrain along the Medial Sumatra Tectonic Zone (Hutchison, 1994).

The Woyla Nappe, consisting of volcanics, carbonates, and imbricated ocean floor materials (Pulunggono and Cameron, 1984; Barber, 2000), collided with West Sumatra during the Late Cretaceous (Wajzer et al., 1991). The subduction of the Indo–Australian Plate beneath Sundaland commenced in the Cenozoic and was important for Cenozoic mineralization.
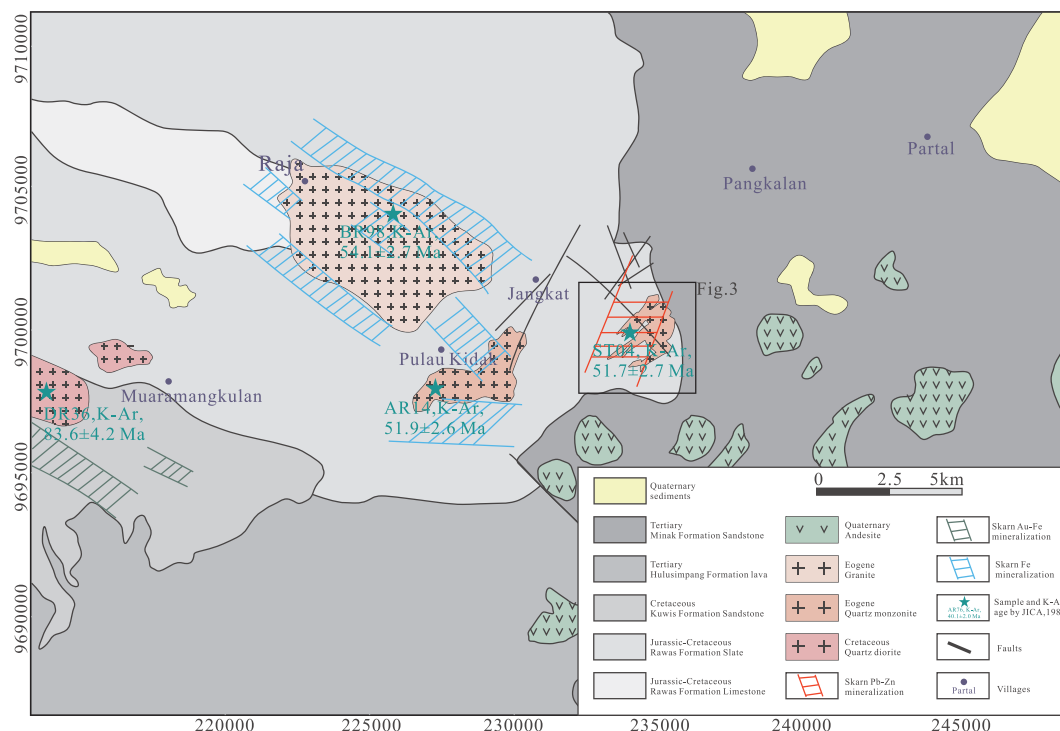
Fig. 2. Sketch map of south Sumatra showing the location of the Tuboh deposit (modified from JICA, 1986, 1987, 1988; Suwarna et al., 1989; Prayogo, 2009; Abidin, 2010).

The Tuboh Pb–Zn–Ag polymetallic deposit is located in the West Sumatra Terrain and is related to collision of the Woyla Nappe and subduction of Indo–Australian Plate. The Woyla Nappe thrusted over along the western margin of Sumatra and resulted in the formation of the Sumatran Fault System (Wajzer et al., 1991; McCarthy, 1997). The Indian Plate subducted beneath Sumatra, which induced arc magmatism along the Barisan Range (Curray et al., 1979; Curray, 1989; McCarthy and Elders, 1997). These intrusions, which range from early Eocene (60–50 Ma) to Miocene–Pliocene (20–5 Ma) (Cobbing, 2005, and references therein), are calc–alkaline, I-type, subduction-related arc granites associated with skarn and porphyry deposits (Beddoe-Stephens et al., 1987; van Leeuwen et al., 1987; JICA, 1988; Imtihanah, 2000; Susanto and Suparka, 2012; Maryono et al., 2014; Hu et al., 2014).

3. Deposit geology

The Tuboh deposit is situated in the southeastern part of Jangkat District, Musi Rawas Regency, Lubuklinggau, South Sumatra, Indonesia. The ore bodies are hosted by limestone of the Jurassic–lower Cretaceous Rawas Formation (Fig. 2; JICA, 1987; Suwarna et al., 1989; Prayogo, 2009). The exposed strata in ore field are dominated by the Rawas Formation, the Cretaceous Kuwis Formation, and the Tertiary Hulusimpang and Minak Formations. Quaternary sediments are partly present and unconformably overlie above these strata (Fig. 2).

The lithology of the Rawas Formation is dominated by limestones and slates with minor andesitic–basaltic lava, tuffs, and volcaniclastic sandstones. The Rawas Formation has undergone thermal metamorphism and skarn mineralization owing to granite intrusion (JICA, 1987; Abidin, 2010). The Kuwis Formation is composed mainly of sandstone, shale, slate, and limestone with minor andesitic–basaltic lava that have undergone relatively low-grade metamorphism. The Hulusimpang Formation is extensively exposed at the southwestern margin of the study area and contains andesitic–dacitic pyroclastics and lavas. The Minak Formation consists primarily of sandstone with minor mudstone, siltstone, dacitic tuff, and limestone.

Exposed intrusions include granite, quartz diorite, and quartz

monzonite (Fig. 2; JICA, 1987; Prayogo, 2009). The Muaramangkulan quartz diorite (83.6 ± 4.2 Ma) is emplaced in the Kuwis Formation and has resulted in skarn Fe and Au mineralization. Two intrusions of quartz monzonite intruded the Rawas Formation at Pulaukidak and Tuboh, respectively. The Pulaukidak quartz monzonite (51.9 ± 2.7 Ma) is related to skarn Fe mineralization, and the Jangkat quartz monzonite (51.7 ± 2.7 Ma) is associated with skarn Pb–Zn–Cu–Ag mineralization in the Tuboh deposit. The emplacements of the Raja granite (54.1 ± 2.7 Ma) caused the skarn Fe mineralization along the Rawas Formation. Numerous Quaternary andesite intrusions are present in the Minak Formation in the southeastern part of the mine (Fig. 2).

Two groups of folding structure are defined in the Tuboh deposit. An isoclinal fold occurs at the northern part of the area, and a synclinorium is present near Raja. Two groups of faults, one striking NW–SE and the other striking NE–SW, are widespread in the Tuboh deposit (Fig. 2). These faults controlled the emplacement of plutonic rock and mineralization.

The mineralization in the Tuboh deposit have a close relationship with the Rawas Formation, the Eocene Jangkat quartz monzonite, and NE–SW-trending faults. The Rawas Formation were intruded by the Eocene Jangkat quartz monzonite. This intrusion has been identified on the surface and at different underground levels, and has contacts with ore veins (Figs. 2, 3; JICA, 1987; Prayogo, 2009). Due to emplacement of the intrusion, the limestone of the Tuboh deposit recrystallized into marble. The host rock suffered skarnization, chloritization, silicification, and carbonation alteration.

Drillings by the PT Galtam Co. revealed that the orebodies mainly occur as wedge-shaped lenses within the contact zone between the intrusion and marble (Figs. 3, 4A). The interlayer gliding zones controlled by NE–SW-trending faults are the most favorable for mineralization in the Tuboh deposit (Prayogo, 2009). Seven (named vein A to E) NE–SW-trending (190–220°) and steeply E–W-dipping (~70°) ore veins are identified by drillings in the Tuboh deposit, and are in parallel NW-trending distribution (Fig. 3; Prayogo, 2009). These ore veins share distinct and diffusive boundaries with wall rocks/intrusions (Fig. 4A) and are more than 900 m long, 0–10 m wide, and have high-grade Pb,
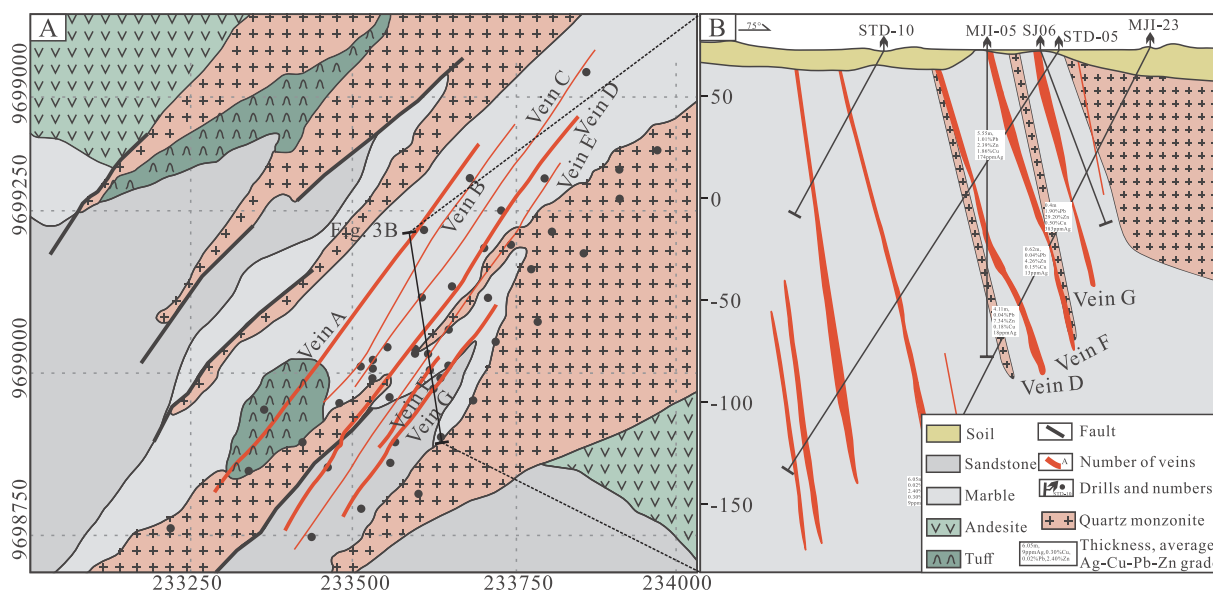
Fig. 3. A. Geological map of the Tuboh deposit. B. Cross-section of the I–I′ prospecting line (modified from JICA, 1988; Suwarna et al., 1989; Prayogo, 2009).

Zn Cu, and Ag at maximum grade of 17.96 wt%, 36.40, wt.%, 5.16 wt%, and 220 ppm, respectively (Table 1; Prayogo, 2009).

Among them, vein A distributes on the northwest of the Tuboh deposit, and contains 3 economic orebodies. The major orebody occurs as veins and lenses between level 40 m to level 280 m, and has a maximum thickness of 6.35 m, and from 10 to 100 m in length (Prayogo, 2009). Ores in vein A contain 0.14 Mt metals with average grades of 115 ppm Ag, 0.12 wt% Cu, 3.66 wt% Pb, and 6.78 wt% Zn. Vein B distributes to the southeast of vein A and strikes nearly parallel

to it, and contains 4 economic orebodies. Individual orebodies vary between 0.2 and 14.9 m in thickness, and from 10 to 50 m in length. Vein B contains 0.33 Mt metals with average grades of 104 ppm Ag, 0.66 wt% Cu, 1.36 wt% Pb, and 7.28 wt% Zn (Prayogo, 2009).

The sulfide veins occur mainly between the contact zone of marble and the skarn alteration (Fig. 4A). The ore veins distribute in or across the wollastonite skarns (Fig. 4B, D), reflecting that these veins were precipitated generally in the later stage. Hematite is present on the borders of garnets (Fig. 5A). Dark grey, fine-grained quartz (Qz-1) and
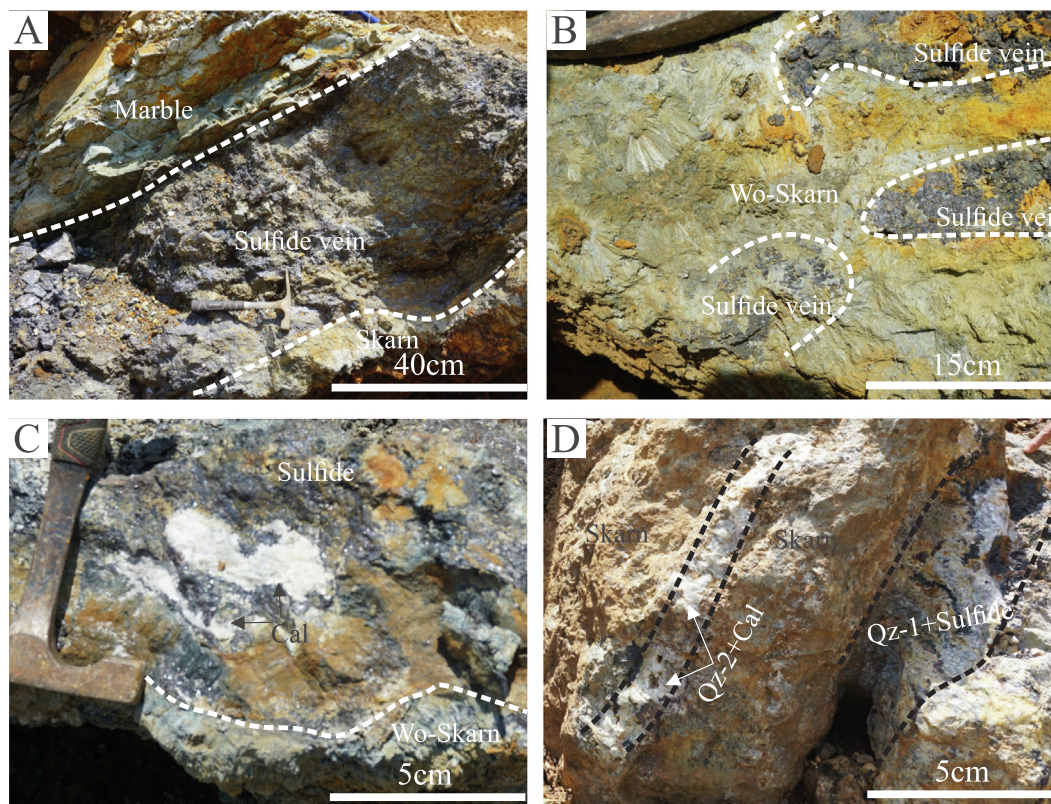
Fig. 4. Photographs of outcrop and hand samples showing textural relationships of the Tuboh deposit. A. Sulfide veins occurring between the footwall of the limestone and the skarn alteration. B. Sulfide veins distributed in wollastonite skarns. C. Calcite and quartz cutting ore minerals. D. Sulfide with quartz-1 andquartz-2 with calcite cutting skarns. Cal: calcite; Ccp: chalcopyrite; Gn: galena; Py: pyrite; Qz: quartz; Sp: sphalerite; Wo: wollastonite.

Table 1
Summary of the Dimension and Characteristics of Major Skarn Veins in the Tuboh Deposit[1].

Vein no.	Strike	Dip	Length(m)	Width (m)	Ag (ppm)	Cu (wt%)	Pb (wt%)	Zn (wt%)	Resources(t)[1]
A	190 ~ 220°	60 ~ 75°	200	0.30 ~ 6.35	2 ~ 1123(1 1 5)	0.00 ~ 5.16(0.12)	0.01 ~ 17.72(3.66)	0.39 ~ 21.42(6.78)	140,393
B	190 ~ 220°	60 ~ 75°	210	0.20 ~ 14.90	0 ~ 355(1 0 4)	0.01 ~ 1.71(0.66)	0.00 ~ 17.96(1.36)	0.43 ~ 24.39(7.28)	339,390
C	190 ~ 220°	60 ~ 65°	250	0.20 ~ 13.55	9 ~ 129(1 0 4)	0.03 ~ 2.01(1.44)	0.09 ~ 9.64(4.86)	1.79 ~ 16.30(8.57)	77,608
D	190 ~ 220°	70 ~ 80°	260	0.15 ~ 4.11	6 ~ 91(18)	0.00 ~ 0.18(0.18)	0.04 ~ 0.50(0.04)	0.31 ~ 20.10(7.34)	75,145
E	190 ~ 220°	60 ~ 75°	200	0.33 ~ 9.50	5 ~ 350(57)	0.00 ~ 3.78(0.55)	0.02 ~ 6.38(0.94)	0.31 ~ 25.00(4.97)	89,814
F	190 ~ 220°	70 ~ 80°	40	0.20 ~ 5.55	13 ~ 174(4 3 3)	0.04 ~ 1.86(0.81)	0.04 ~ 1.25(0.43)	0.85 ~ 9.20(4.25)	11,113
G	190 ~ 220°	70 ~ 80°	100	0.40 ~ 21.00	48 ~ 1220(2 5 1)	0.11 ~ 4.45(0.91)	0.65 ~ 6.90(2.17)	0.17 ~ 36.40(10.05)	58,746

Notes:[1]Data base on 333 classification after Prayogo (2009).

sulfide veins cut the garnet, indicating that the former was precipitated generally during the later stage (Figs. 4C-D, 5B-C, 6A-B). Magnetite, pyrite, and chalcopyrite coexists with sphalerite (Fig. 5D, 6C-D). The chalcopyrite is in symbiosis with pyrrhotite (Fig. 5E, F). Calcite and white, euhedral to subhedral, coarse-grained quartz (Qz-2) cut the ore minerals (Fig. 4C and D), suggesting that the former was deposited during the late hydrothermal stage. The ores occur as massive, banded, and stockwork structures with euhedral half-crystalline, crystalline, interstitial, and exsolution textures.

On the basis of field and petrographic investigations, four stages
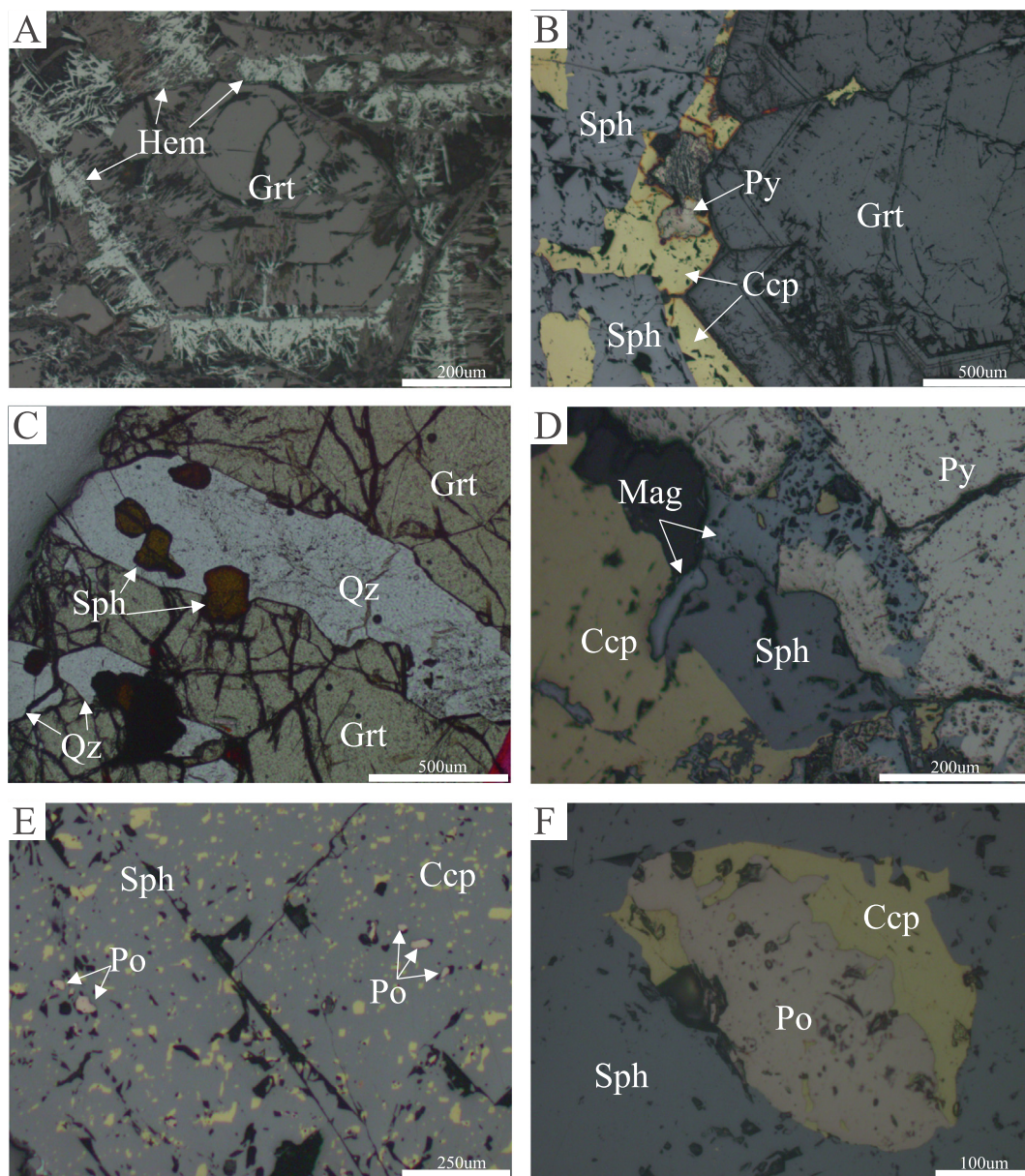
Fig. 5. Reflected-light photomicrographs of the Tuboh deposit. A. Hematite overgrowth on the border of garnet. B. Sulfide veins cutting garnet. C. Quartz and sulfide veins cutting garnet. D. Magnetite, pyrite, and chalcopyrite coexisting with sphalerite. E. Chalcopyrite and pyrrhotite present as diseases in sphalerite. F. Chalcopyrite symbiosis with pyrrhotite in sphalerite. Ccp: chalcopyrite; Grt: garnet; Hem: hematite; Mag: magnetite; Po: pyrrhotite; Py: pyrite; Qz: quartz; Sp: sphalerite.
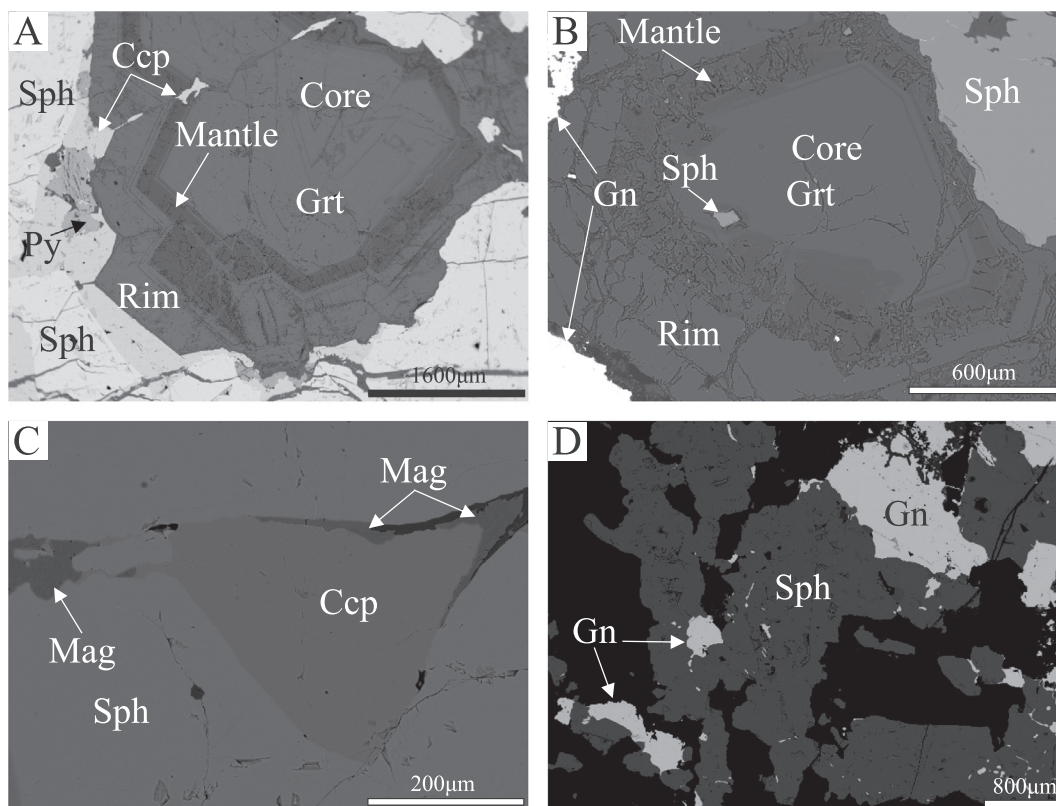
Fig. 6. Back-scattered electron images of the Tuboh deposit. A. Sulfide veins cutting garnet, which shows core–mantle–rim structure. B. Sulfides coexisting with garnet, also showing core-mantle-rim structure. C. Magnetite intergrown with chalcopyrite in sphalerite. D. Galena symbiosis with sphalerite. Ccp: chalcopyrite; Gn: galena; Grt: garnet; Mag: magnetite; Py: pyrite; Qz: quartz; Sp: sphalerite.

were defined for the formation of the Tuboh deposit (Fig. 7): prograde, retrograde, quartz-sulfide, and quartz–calcite stages. The prograde facies are anhydrous minerals with predominant garnet and wollastonite. The quartz-sulfide stage contain quartz, calcite, pyrrhotite, pyrite, chalcopyrite, sphalerite, and galena. The sulfide minerals were precipitated mainly during this stage.

4. Analytical methods and results

4.1. Analytical methods

Representative samples for fluid inclusions and isotope analysis were collected from an open pit. Electron probe microanalysis (EPMA), microthermometric measurements, and S isotope analysis were completed at the State Key Laboratory of Ore Deposit Geochemistry, Institute of Geochemistry, Chinese Academy of Sciences. *In situ* Pb isotope analysis was performed at the State Key Laboratory of Continental Dynamics, Northwest University.

Ore and gangue minerals were analyzed by electron microprobe with wavelength dispersive analysis, which employed a JEOL JXA-8530F Plus electron microprobe with a 1–10 μm beam diameter, 25 kV accelerating potential, and 10 nA probe current. Natural garnet was adopted as the standard for garnet analysis, and the following natural mineral or synthetic metal standards were used for the sulfides: Fe (FeS_2), Cu ($CuFeS_2$), Pb (PbS), Zn (ZnS), S (FeS_2), Co (Co), Bi (Bi), Au (Au), and Ag (Ag). The data were reduced by using the ZAF correction method.

Microthermometric measurements of fluid inclusions were performed by using a Linkam THMS-600 heating–freezing stage attached to a Leica DM2500 microscope. Stage calibration was conducted by using synthetic fluid inclusions distributed by Fluid Inc., USA. The uncertainties of temperature measurements were ± 0.2 °C

for < −70 °C, ± 1 °C for < 100 °C, and ± 2 °C for < 400 °C. The heating/freezing rate was at 10–20 °C/min during the initial runs and was reduced to 0.2 °C/min near the phase transformation. The salinities for aqueous solutions were calculated by using the final ice melting temperatures based on the equation of Bodnar (1993).

Sulfide grains were crushed to 40–60 mesh and were handpicked under a binocular microscope for S isotope analysis. The S isotope ratio was analyzed by the direct oxidation method using a MAT 253 mass spectrometer. GBW 04415 and GBW 04414 were also determined as standards. The analytical uncertainties for $\delta^{34}S$ were better than 0.1‰ (2σ).

In situ Pb isotope analysis for galena was performed by using a RESOlution M-50 laser ablation system (ASI, Australia) connected to a Nu Plasma II multi-collector inductively coupled plasma mass spectrometer (MC-ICP-MS; Nu Instruments, Wrexham, UK), with 9 μm beam diameter, 6 Hz repetition time, and 6 J/cm² energy density. He was serviced as a carrier gas at an uptake rate of 280 mL/min. Each analysis consisted of a background measurement for 30 s followed by 50 s of ablation for signal collection and an additional 40 s of wash time to reduce the memory effects. The ^{205}Tl, $^{204}Hg + ^{204}Pb$, ^{203}Tl, ^{202}Hg, ^{206}Pb, ^{207}Pb, and ^{208}Pb were collected by L1, L2, L3, L4, Ax, H1, and H2 Faraday cups, respectively. Mass fractionation was corrected by normalizing to $^{205}Tl/^{203}Tl = 2.3889$ with an exponential law. PSPT-2, Gn01, and NIST SRM 610 glass were used as internal and external standards, respectively. The isotopic ratios of these standards were reliable and reproducible and showed good agreement with the reference (Chen et al., 2014; Yuan et al., 2015) during the analytical process. Details of the femtosecond-laser ablation (*fs*-LA)-MC-ICP-MS *in situ* Pb isotope analysis and instrument parameters are available in Bao et al. (2017).
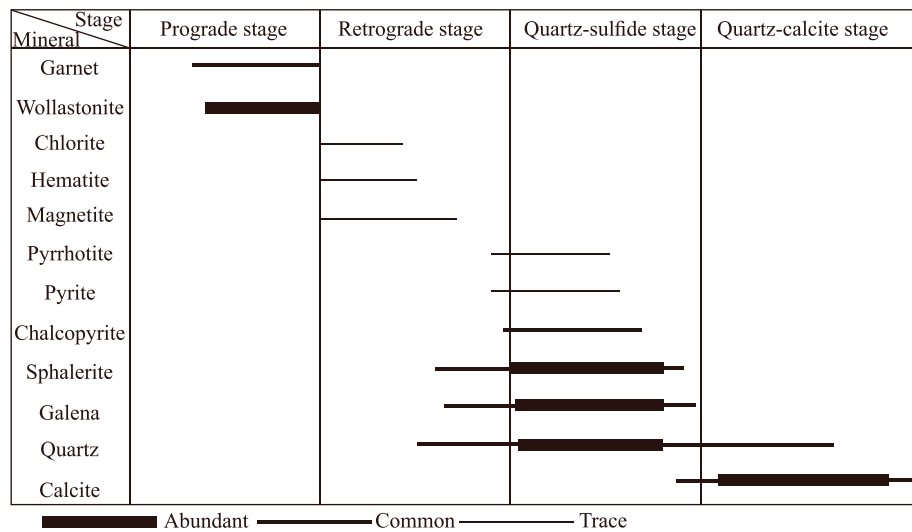
Fig. 7. Paragenetic sequence of mineralization/alteration in the Tuboh deposit.

4.2. Results

4.2.1. Chemistry of minerals

Garnet and ore minerals of the Tuboh deposit were selected for major element analyses by EPMA (Fig. 6). The garnet composition and calculated end-member are given in Table 2. The compositions of the ore minerals are presented in Table 3.

The garnet contains high Fe, Al, and Ca, whereas the Cr, Mn, and Mg are relatively low. Back-scattered electron (BSE) images of individual garnet grains show core–mantle–rim texture (Fig. 6A, B). The chemical compositions of the core and rim are $Adr_{94.73-98.02}Grs_{0.93-4.35}Sps + Alm_{0.80-1.11}$ and $Adr_{95.34-98.58}Grs_{0.82-3.90}Sps + Alm_{0.48-0.77}$, respectively. These results indicate that core and rim are rich in andradite. The mantle is rich in grossularite with a composition of $Adr_{37.89-50.83}Grs_{47.22-58.93}Sps + Alm_{1.95-3.08}$.

The pyrite contains variable amounts of Cu, Co, and Ag at maximum

Table 2
Representative Microprobe Analyses of Garnet from the Tuboh Deposit.

Position	Sample no.	SiO₂	TiO₂	Al₂O₃	Cr₂O₃	Fe₂O₃	MnO	MgO	CaO	Na₂O	K₂O	Total	And	Gro	Pyr	Spe	Alm
Core																	
	LM-15-01	34.80	0.00	0.00	0.00	31.24	0.38	0.01	33.17	0.00	0.00	99.59	97.76	1.00	0.19	0.89	0.16
	LM-15-02	34.47	0.00	0.00	0.00	30.94	0.31	0.05	33.12	0.00	0.00	98.89	97.22	1.84	0.00	0.74	0.19
	LM-15-03	34.84	0.00	0.13	0.00	31.22	0.34	0.00	33.23	0.00	0.00	99.75	98.02	1.10	0.04	0.79	0.04
	LM-15-04	34.58	0.00	0.00	0.00	31.07	0.36	0.01	33.18	0.00	0.00	99.20	97.73	1.39	0.01	0.85	0.02
	LM-15-05	34.96	0.00	0.51	0.00	30.25	0.38	0.00	33.32	0.01	0.00	99.43	94.73	4.35	0.00	0.90	0.02
	LM-11-01	34.99	0.00	0.55	0.00	30.43	0.34	0.00	33.20	0.03	0.00	99.53	95.72	3.44	0.00	0.81	0.02
	LM-11-02	35.02	0.04	0.55	0.00	30.29	0.34	0.00	33.36	0.03	0.01	99.63	94.83	4.31	0.07	0.80	0.00
	LM-11-03	34.88	0.00	0.67	0.02	30.34	0.34	0.02	33.12	0.00	0.00	99.40	95.58	3.49	0.00	0.80	0.07
	LM-11-04	34.96	0.00	0.43	0.00	30.60	0.38	0.00	33.02	0.00	0.00	99.39	96.74	2.35	0.00	0.91	0.00
	LM-11-05	34.21	0.00	0.24	0.00	31.14	0.36	0.00	33.00	0.00	0.00	98.93	97.86	0.93	0.13	0.84	0.23
	LM-11-06	34.55	0.02	0.17	0.00	30.87	0.37	0.03	33.01	0.04	0.00	99.06	97.07	1.82	0.00	0.88	0.23
	LM-11-07	34.25	0.00	0.29	0.00	30.38	0.38	0.00	33.13	0.00	0.00	98.43	95.20	3.62	0.12	0.89	0.18
	LM-11-08	34.75	0.00	0.42	0.03	30.36	0.38	0.03	33.20	0.03	0.00	99.18	95.23	3.65	0.04	0.90	0.08
Mantle																	
	LM-15-01	37.04	0.00	10.91	0.00	17.04	0.83	0.00	34.53	0.00	0.00	100.34	50.83	47.22	0.00	1.85	0.10
	LM-15-02	37.22	0.02	12.56	0.00	14.76	1.00	0.00	34.55	0.02	0.01	100.12	43.90	53.83	0.00	2.23	0.04
	LM-15-03	37.08	0.00	12.61	0.00	14.55	1.02	0.00	34.74	0.00	0.00	100.01	42.79	54.77	0.00	2.27	0.18
	LM-11-01	36.88	0.02	11.49	0.00	15.87	0.97	0.01	34.45	0.02	0.00	99.72	47.28	50.44	0.00	2.18	0.10
	LM-11-02	36.66	0.03	11.24	0.00	16.11	0.88	0.00	34.44	0.00	0.00	99.36	48.31	49.71	0.00	1.98	0.00
	LM-11-03	37.02	0.00	12.44	0.01	14.63	1.04	0.00	34.51	0.00	0.00	99.65	43.51	54.03	0.05	2.32	0.05
	LM-11-04	36.68	0.00	12.13	0.00	14.98	1.04	0.01	34.53	0.00	0.00	99.38	44.52	53.10	0.00	2.33	0.05
	LM-11-05	37.24	0.00	13.49	0.00	13.45	1.09	0.00	34.59	0.00	0.00	99.87	39.45	57.74	0.13	2.43	0.25
	LM-11-06	37.45	0.00	14.33	0.00	12.91	1.32	0.03	34.54	0.05	0.00	100.62	37.89	58.93	0.10	2.93	0.15
Rim																	
	LM-15-01	34.26	0.00	0.00	0.01	31.00	0.24	0.00	33.37	0.04	0.00	98.93	97.10	2.20	0.05	0.57	0.06
	LM-15-02	34.32	0.00	0.34	0.02	30.51	0.24	0.01	33.30	0.00	0.00	98.74	95.86	3.46	0.00	0.57	0.05
	LM-15-03	34.49	0.00	0.00	0.00	31.00	0.29	0.00	33.39	0.00	0.00	99.16	97.15	2.18	0.00	0.67	0.00
	LM-15-04	34.98	0.00	0.00	0.00	31.39	0.23	0.00	33.32	0.00	0.00	99.92	98.42	0.88	0.08	0.53	0.08
	LM-15-05	34.45	0.00	0.00	0.00	30.96	0.29	0.02	33.43	0.00	0.00	99.15	96.83	2.45	0.00	0.68	0.04
	LM-15-06	34.88	0.00	0.42	0.01	30.55	0.29	0.00	33.32	0.07	0.00	99.53	95.95	3.36	0.00	0.68	0.00
	LM-11-01	34.76	0.00	0.58	0.00	30.30	0.32	0.03	33.23	0.00	0.00	99.22	95.34	3.90	0.00	0.76	0.00
	LM-11-02	34.61	0.00	0.00	0.01	31.19	0.28	0.00	33.09	0.04	0.00	99.23	98.38	0.82	0.00	0.66	0.11
	LM-11-03	35.48	0.00	0.00	0.00	31.16	0.20	0.00	33.22	0.00	0.00	100.05	98.33	1.19	0.00	0.48	0.00
	LM-11-04	35.27	0.01	0.00	0.01	31.24	0.23	0.00	33.20	0.00	0.00	99.96	98.58	0.83	0.00	0.55	0.00

Notes: Alm = almandine, And = andradite, Gro = grossularite, Pyr = pyrope, Spe = spessartine.

Table 3
Representative Microprobe Analyses of ore minerals in the Tuboh Deposit.

Mineral	Sample no.	Fe	S	Cu	Zn	Co	Au	Ag	Bi	Pb	Total
Pyrite											
	LM-11-01	44.94	50.51	1.48	B.D.L	B.D.L	B.D.L	0.18	B.D.L	B.D.L	97.36
	LM-11-02	45.76	52.26	0.57	B.D.L	B.D.L	B.D.L	0.18	B.D.L	B.D.L	99.15
	LM-11-03	45.76	51.47	0.28	B.D.L	0.09	B.D.L	0.12	B.D.L	B.D.L	97.76
	LM-11-04	45.59	51.30	0.30	B.D.L	0.10	B.D.L	0.12	B.D.L	B.D.L	97.45
	LM-11-05	45.70	51.54	0.25	B.D.L	0.10	B.D.L	0.12	B.D.L	B.D.L	97.79
	LM-18-01	46.35	53.85	B.D.L	B.D.L	0.05	B.D.L	B.D.L	B.D.L	B.D.L	100.33
	LM-18-02	46.77	53.54	B.D.L	B.D.L	0.03	B.D.L	B.D.L	B.D.L	B.D.L	100.43
	LM-18-03	45.54	52.17	1.69	B.D.L	0.03	B.D.L	B.D.L	B.D.L	B.D.L	99.57
	LM-18-04	46.43	53.67	B.D.L	B.D.L	0.07	B.D.L	B.D.L	B.D.L	B.D.L	100.33
	LM-18-05	46.69	53.52	B.D.L	B.D.L	0.03	B.D.L	B.D.L	B.D.L	B.D.L	100.27
	LM-18-06	46.38	53.66	0.07	B.D.L	0.04	B.D.L	B.D.L	B.D.L	B.D.L	100.22
	LM-18-07	46.82	53.58	B.D.L	B.D.L	0.03	B.D.L	B.D.L	B.D.L	B.D.L	100.55
Pyrrhotite											
	LM-04-01	60.04	40.98	0.23	B.D.L	B.D.L	B.D.L	B.D.L	B.D.L	B.D.L	101.40
	LM-04-02	59.04	39.20	0.21	B.D.L	0.32	B.D.L	B.D.L	B.D.L	B.D.L	98.85
	LM-04-03	58.95	39.06	0.23	B.D.L	0.34	B.D.L	B.D.L	B.D.L	B.D.L	98.68
	LM-04-04	58.95	39.34	0.14	B.D.L	0.32	B.D.L	B.D.L	B.D.L	B.D.L	98.82
	LM-04-05	59.33	38.96	0.13	B.D.L	0.42	B.D.L	B.D.L	B.D.L	B.D.L	99.03
	LM-04-06	46.81	53.24	B.D.L	B.D.L	0.05	B.D.L	B.D.L	B.D.L	B.D.L	100.22
Chalcopyrite											
	LM-11-01	31.08	35.88	35.01	0.06	B.D.L	B.D.L	B.D.L	B.D.L	B.D.L	102.09
	LM-11-02	30.86	35.97	35.06	0.12	B.D.L	B.D.L	B.D.L	B.D.L	B.D.L	102.05
	LM-11-03	31.01	35.98	34.70	0.10	B.D.L	B.D.L	B.D.L	B.D.L	B.D.L	101.94
	LM-11-04	31.14	35.84	34.95	0.08	B.D.L	B.D.L	B.D.L	B.D.L	B.D.L	102.14
	LM-11-05	31.05	36.07	34.93	0.08	B.D.L	B.D.L	B.D.L	B.D.L	B.D.L	102.44
	LM-11-06	31.16	35.84	34.89	0.09	B.D.L	B.D.L	B.D.L	B.D.L	B.D.L	102.09
	LM-11-07	31.05	35.91	34.55	0.11	B.D.L	B.D.L	B.D.L	B.D.L	B.D.L	101.75
	LM-15-01	30.98	35.71	34.84	0.12	B.D.L	B.D.L	B.D.L	B.D.L	B.D.L	101.66
	LM-15-02	30.92	35.69	35.02	0.08	B.D.L	B.D.L	B.D.L	B.D.L	B.D.L	101.87
	LM-15-03	31.03	35.35	34.81	0.10	B.D.L	B.D.L	B.D.L	B.D.L	B.D.L	101.38
	LM-15-04	31.15	35.87	34.81	0.04	B.D.L	B.D.L	B.D.L	B.D.L	B.D.L	102.10
	LM-15-05	31.21	35.56	34.65	B.D.L	B.D.L	B.D.L	B.D.L	B.D.L	B.D.L	101.57
	LM-15-06	31.30	36.08	34.93	0.05	B.D.L	B.D.L	B.D.L	B.D.L	B.D.L	102.54
Sphalerite											
	LM-02-01	10.33	33.46	B.D.L	55.21	B.D.L	B.D.L	B.D.L	B.D.L	B.D.L	99.12
	LM-02-02	10.27	33.81	0.08	55.06	B.D.L	B.D.L	B.D.L	B.D.L	B.D.L	99.36
	LM-02-03	10.69	33.80	B.D.L	54.74	B.D.L	B.D.L	B.D.L	B.D.L	B.D.L	99.39
	LM-05-01	3.56	33.43	B.D.L	63.16	B.D.L	B.D.L	B.D.L	B.D.L	B.D.L	100.18
	LM-05-02	4.48	33.30	B.D.L	61.88	B.D.L	B.D.L	B.D.L	B.D.L	B.D.L	99.77
	LM-05-03	4.46	33.10	B.D.L	61.86	B.D.L	B.D.L	B.D.L	B.D.L	B.D.L	99.59
	LM-05-04	3.16	33.62	B.D.L	63.58	B.D.L	B.D.L	B.D.L	B.D.L	B.D.L	100.36
	LM-05-05	4.69	33.36	B.D.L	61.68	B.D.L	B.D.L	B.D.L	B.D.L	B.D.L	99.79
	LM-05-06	4.86	33.30	B.D.L	61.61	B.D.L	B.D.L	B.D.L	B.D.L	B.D.L	99.99
	LM-10-01	7.01	33.46	B.D.L	58.90	B.D.L	B.D.L	B.D.L	B.D.L	B.D.L	99.57
	LM-10-02	6.87	32.95	B.D.L	59.01	B.D.L	B.D.L	B.D.L	B.D.L	B.D.L	98.91
	LM-10-03	6.75	33.19	B.D.L	59.25	B.D.L	B.D.L	B.D.L	B.D.L	B.D.L	99.31
	LM-10-04	7.73	33.39	B.D.L	58.05	B.D.L	B.D.L	B.D.L	B.D.L	B.D.L	99.18
	LM-10-05	6.40	33.45	B.D.L	59.33	B.D.L	B.D.L	B.D.L	B.D.L	B.D.L	99.20
	LM-10-06	5.93	33.33	B.D.L	59.31	B.D.L	B.D.L	B.D.L	B.D.L	B.D.L	98.59
	LM-15-01	9.55	33.68	B.D.L	55.63	B.D.L	B.D.L	B.D.L	B.D.L	B.D.L	99.15
	LM-15-02	10.03	33.40	B.D.L	55.39	B.D.L	B.D.L	B.D.L	B.D.L	B.D.L	98.90
	LM-15-03	9.87	33.73	0.06	55.89	B.D.L	B.D.L	B.D.L	B.D.L	B.D.L	99.59
	LM-15-04	9.42	33.36	B.D.L	56.39	B.D.L	B.D.L	B.D.L	B.D.L	B.D.L	99.31
	LM-15-05	9.36	33.48	B.D.L	56.34	B.D.L	B.D.L	B.D.L	B.D.L	B.D.L	99.24
	LM-15-06	9.85	33.73	0.06	56.11	B.D.L	B.D.L	B.D.L	B.D.L	B.D.L	99.92
	LM-15-07	9.47	33.73	B.D.L	56.46	B.D.L	B.D.L	B.D.L	B.D.L	B.D.L	99.68
	LM-15-08	9.53	33.64	B.D.L	56.82	B.D.L	B.D.L	B.D.L	B.D.L	B.D.L	100.01
	LM-15-09	9.62	33.45	B.D.L	56.54	B.D.L	B.D.L	B.D.L	B.D.L	B.D.L	99.76
	LM-15-10	9.63	34.20	B.D.L	56.47	B.D.L	B.D.L	B.D.L	B.D.L	B.D.L	100.48
	LM-15-11	9.38	34.30	B.D.L	57.04	B.D.L	B.D.L	B.D.L	B.D.L	B.D.L	100.90
	LM-15-12	9.46	33.55	B.D.L	56.14	B.D.L	B.D.L	B.D.L	B.D.L	B.D.L	99.17
Galena											
	LM-02-01	B.D.L	13.53	B.D.L	B.D.L	B.D.L	B.D.L	0.13	0.39	86.10	100.30
	LM-02-02	B.D.L	13.55	B.D.L	B.D.L	B.D.L	B.D.L	0.08	0.51	86.26	100.46
	LM-05-01	B.D.L	13.85	B.D.L	B.D.L	B.D.L	B.D.L	0.71	1.77	84.42	100.77
	LM-05-02	B.D.L	13.63	B.D.L	B.D.L	B.D.L	B.D.L	0.69	2.00	83.74	100.11
	LM-05-03	0.06	13.73	B.D.L	B.D.L	B.D.L	B.D.L	0.68	1.69	84.29	100.47
	LM-05-04	B.D.L	13.57	B.D.L	B.D.L	B.D.L	B.D.L	0.50	1.55	84.14	99.80
	LM-05-05	B.D.L	13.75	B.D.L	B.D.L	B.D.L	B.D.L	0.54	1.45	84.98	100.75
	LM-05-06	B.D.L	13.69	B.D.L	B.D.L	B.D.L	B.D.L	0.67	1.84	84.10	100.35
	LM-05-07	B.D.L	13.50	B.D.L	B.D.L	B.D.L	B.D.L	0.61	1.55	83.11	98.79

Table 3 (*continued*)

Mineral	Sample no.	Fe	S	Cu	Zn	Co	Au	Ag	Bi	Pb	Total
	LM-05-08	B.D.L	13.79	B.D.L	B.D.L	B.D.L	B.D.L	0.64	1.41	83.70	99.59
	LM-10-01	0.05	13.67	B.D.L	0.13	B.D.L	B.D.L	0.96	2.22	83.23	100.28
	LM-10-02	B.D.L	13.60	B.D.L	0.10	B.D.L	B.D.L	0.94	2.39	81.90	98.96
	LM-10-03	0.06	13.65	B.D.L	B.D.L	B.D.L	B.D.L	0.96	2.27	82.36	99.35
	LM-10-04	B.D.L	13.89	B.D.L	0.12	B.D.L	B.D.L	0.97	2.46	82.98	100.45
	LM-10-05	0.06	13.82	B.D.L	B.D.L	B.D.L	B.D.L	0.83	2.13	83.24	100.14
	LM-15-01	0.05	13.60	B.D.L	B.D.L	B.D.L	B.D.L	0.39	1.15	84.31	99.52
	LM-15-02	0.05	13.45	B.D.L	B.D.L	B.D.L	B.D.L	0.42	1.18	84.29	99.41
	LM-15-03	0.10	13.60	B.D.L	B.D.L	B.D.L	B.D.L	0.43	1.26	84.65	100.06
	LM-15-04	0.10	13.87	B.D.L	B.D.L	B.D.L	B.D.L	0.55	1.46	83.85	99.85
	LM-15-05	0.10	13.51	B.D.L	0.25	B.D.L	B.D.L	0.60	1.68	84.32	100.46
	LM-15-06	B.D.L	13.66	B.D.L	0.42	B.D.L	B.D.L	0.55	1.14	84.59	100.43
	LM-15-07	B.D.L	13.63	B.D.L	B.D.L	B.D.L	B.D.L	0.13	0.51	85.56	99.85
	LM-15-08	0.06	13.54	B.D.L	B.D.L	B.D.L	B.D.L	0.25	0.70	85.02	99.55

Notes: B.D.L = below detect limit.

concentrations of 1.48 wt%, 0.10 wt%, and 0.18 wt%, respectively. However, the concentrations of Zn, Pb, and Bi are below the detection limit.

The pyrrhotite includes variable amounts of Cu and Co at maximum concentrations of 0.23 wt% and 0.42 wt%, respectively. The concentrations of Ag, Zn, Pb, and Bi are below the detection limit.

The chalcopyrite has variable amounts of Zn and Ag, at 0.03–0.28 wt% and 0.04–0.11 wt%, respectively. However, the concentrations of Co, Bi, and Pb are below the detection limit.

The sphalerite is totally opaque owing to widespread chalcopyrite disease. The concentration of Fe in the sphalerite is variable, ranging from 5.93 to 11.54 wt%, and shows a negative correlation with Zn. The concentration of Cu in sphalerite ranges from 0.06 to 1.70 wt%; Co, Ag, Bi, and Pb are below the detection limit.

The galena contains variable amounts of Fe, Zn, Ag, and Bi and excludes Cu and Co. The concentrations of Fe and Zn are 0.05–0.14 wt% and 0.10–0.42 wt%, respectively. Those of Ag and Bi are 0.05–0.14 wt% and 0.24–2.46 wt%, respectively.

4.2.2. Fluid inclusions studies

Fluid inclusions were selected from the gangue minerals in the Tuboh deposit. All chosen thin sections are rich in primary inclusions that present as individuals or assemblages with elliptical, irregular, negative crystalline, or rhombic shapes (Fig. 8). Secondary inclusions occur as clusters or trails and were not analyzed during microthermometric measurement. Two types of primary fluid inclusions were identified at room temperature. Type 1 includes two-phase inclusions that contain liquid and vapor H_2O phases (L_{H_2O}–V_{H_2O}) generally greater than 5 µm in diameter. Type 2 contains liquid-only aqueous inclusions (L_{H_2O}).

Measurements were performed mainly on type 1 two-phase inclusions and covered all three ore-forming stages. All inclusions were homogenized into the liquid phase during heating. The measurement data are listed in Table 4 and illustrated in Fig. 9.

The fluid inclusions measured from garnet in the prograde stage included total homogenization temperatures of 380–450 °C, with a peak at 417 °C. The final ice melting temperature was −6.0 to −18.6 °C, corresponding to salinities of 9.21 to 21.4 wt% NaCl equivalent, with a peak at 16.08 wt% NaCl equivalent.

The fluid inclusions in the quartz-sulfide stage were studied from quartz intergrown with sulfide. The total homogenization temperatures ranged from 337 to 420 °C, with an average of 381 °C. The final ice melting temperature was between −4.0 and −7.5 °C, and the calculated salinities were 6.45 to 11.1 wt% NaCl equivalent, with an average of 8.04 wt% NaCl equivalent.

The fluid inclusions in the post-ore stage were chosen from quartz and calcite. The final homogenization temperatures and salinities of inclusions in the quartz were 151 to 266 °C, and 0.35 to 4.80 wt% NaCl equivalent, respectively. Those in the calcite were 167 to 219 °C, and 0.35 to 7.45 wt% NaCl equivalent, respectively.

4.2.3. S–Pb isotopes

The S isotopic ratios of the sphalerite, chalcopyrite, and galena are listed in Table 5. The $\delta^{34}S$ values of the sphalerite ranged from −0.42 to 2.53‰, with an average value of 1.03‰ (n = 8). Those of the chalcopyrite were −1.09 to −0.44‰, with an average value of −0.66‰ (n = 3). Those of the galena were −2.44 to 0.91‰, with an average value of −0.90‰ (n = 8).

The *in-situ* Pb isotope compositions of galena yielded $^{206}Pb/^{204}Pb$ ratios of 18.342 to 18.370, with an average of 18.358; $^{207}Pb/^{204}Pb$ ratios of 15.576 to 15.599, with an average of 15.587; and $^{208}Pb/^{204}Pb$ ratios of 38.369 to 38.430, with an average of 38.399 (Table 6).

5. Discussion

5.1. Sources of S and Pb

The $\delta^{34}S$ values of sulfide can reveal the sources of S in ore-forming fluids (Ohmoto, 1986). Sphalerite and chalcopyrite are richer than galena in heavy S isotopes (Fig. 10), indicating that the former two minerals are equilibrated with the ore fluids (Kajiwara and Krouse, 1971). The lack of sulfates in the Tuboh deposit suggests that the $\delta^{34}S$ values of sulfide could represent the bulk S isotopic ratios of the ore-forming fluids (Ohmoto and Rye, 1979). The $\delta^{34}S$ values show a narrow range with minor variation, demonstrating that the S originated from a single homogeneous source. The values were from −2.44 to +2.52‰, with an average of −0.04‰, and are consistent with magmatic S (0 ± 3‰; Ohmoto, 1986; Ohmoto and Rye, 1979; Ripley, 1986; Bonsall et al., 2011). Therefore, the S in the sulfides was derived from magmatic S.

Owing to negligible U and Th and high Pb concentrations in the sulfide minerals, the Pb isotopic compositions of the given minerals can represent the Pb source (Zartman and Doe, 1981; Carr et al., 1995; Zhou et al., 2013). The restricted range of Pb isotopic ratios in the Tuboh deposit indicate it precipitated from a single homogeneous Pb source or Pb mixed from more isotopically heterogeneous sources. For comparison, the Pb isotope ratios of whole-rock samples from the Indian Ocean midocean ridge basalt (MORB; Ito et al., 1987) and the Sumatra mantle and basement (Gasparon and Varne, 1998) were plotted against data obtained in this study in $^{208}Pb/^{204}Pb$ versus $^{206}Pb/^{204}Pb$ and $^{207}Pb/^{204}Pb$ versus $^{206}Pb/^{204}Pb$ diagrams (Zartman and Doe, 1981; Fig. 11).

The Pb isotope compositions of galena from the Tuboh deposit are homogeneous and fall close to the orogenic growth curve, indicating a mixed origin of mantle and crust. Galena enriched in radiogenic Pb is remarkably different from Indian Ocean MORB. The Pb isotopic ratio of
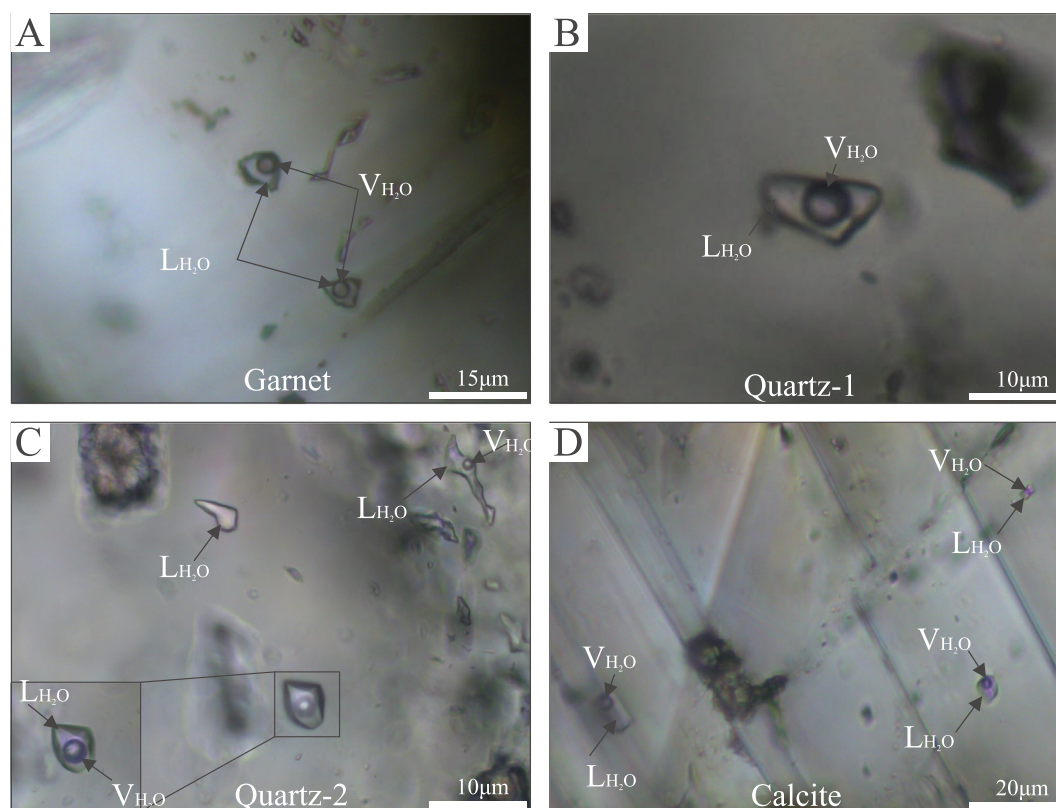
Fig. 8. Photomicrographs of fluid inclusions in the Tuboh deposit. A. Two-phase, liquid-dominant aqueous inclusions in garnet from the prograde stage. B. Two-phase, liquid-dominant aqueous inclusions in quartz-1 from the quartz-sulfide stage. C. Two-phase, liquid-dominant aqueous inclusions in quartz-2 from the quartz–calcite stage. D. Two-phase, liquid-dominant aqueous inclusions in calcite from the quartz–calcite stage. L: liquid; V: vapor.

the Tuboh deposit is slightly rich in radiogenic Pb isotope ratios and falls between Sumatra mantle and basement, but is close to that in mantle. This suggests that the Pb mainly originated from mantle.

Notably, the Sr isotope composition of the Eocene Jangkat quartz monzonite is 0.70451 (JICA, 1987), indicating that the intrusion mainly originated from mantle. The Sr isotopic ratios of related skarns are 0.70588–0.70721 and are located between the slate of the Rawas Formation (0.73042) and the intrusion (JICA, 1987). In addition, the Eocene Jangkat quartz monzonite has close spatial genetic relationship with the Tuboh deposit, as this intrusion has been identified in ore field, and has varying degrees of contact with ore veins at different underground levels (Figs. 2, 3; JICA, 1987; Prayogo, 2009). Therefore, these signatures suggest that the Eocene Jangkat quartz monzonite is the source of the Pb and associated metals in the Tuboh deposit.

5.2. Evolution of redox state and ore-forming fluids

The redox state can be recorded by garnets (Meinert et al., 2005). Andradite represents oxidized environments, whereas grossularite indicates reduced conditions (Kwak, 1987; Newberry, 1983; Einaudi et al., 1981). At Tuboh, garnet and wollastonite are formed in the prograde stage. Moreover, the dominant garnet is andradite, and the stoichiometry calculation revealed that Fe is dominant in the oxidized state (Fe^{3+}) in the garnet. Therefore, the chemical compositions of the garnet indicate that the skarn was formed under an oxidized environment. In addition, the retrograde stage is characterized by magnetite and hematite, which suggests the oxidized conditions.

Although the andradite ($Adr_{37-99}Grs_{1-59}$), hematite, and magnetite show that the Tuboh deposit was formed under oxidized conditions. Minor grossularite zone ($Adr_{37-50}Grs_{47-58}$) occur in mantle of garnet grains (Fig. 6A, B), which may reflect the locally reduced environment in formation of skarn, as the ore-forming fluids probably interacted with some reduced limestone and slate of the Rawas Formation.

The chemical analyses of the sphalerite indicate Fe concentrations of 5.93 to 11.54 wt% and show a negative correlation with Zn, indicating the substitution of Fe for Zn (Herzig, 1988). The physico-chemical conditions of the sphalerite crystallization were estimated on the basis of the Fe content (Scott and Barnes, 1971; Keith et al., 2014). The temperatures for sphalerite precipitation are 270–392 °C, which is similar to the homogenization temperatures of quartz inclusions in the

Table 4
Summary of Microthermometric Data and relative Parameters for Fluid Inclusions from the Tuboh Deposit.

Stage	Host mineral	FI type	Size/μm	$T_{m, ice}$ (°C)	T_h (°C)		Salinity[2](wt.%NaCl eq.)	
					Value	Mean value[1]	Value	Mean value[1]
Prograde stage	Garnet	Type 1	5 ~ 28	−6 ~ −18.6	380 ~ 450	417(18)	9.21 ~ 21.4	16.08(17)
Quartz-sulfide stage	Quartz-1	Type 1	7 ~ 20	−4.0 ~ −7.5	337 ~ 420	381(19)	6.45 ~ 11.1	8.04(17)
Quartz-calcite stage	Quartz −2	Type 1	7 ~ 25	−0.2 ~ −2.9	151 ~ 266	196(20)	0.35 ~ 4.8	2.25(18)
	Calcite	Type 1	5 ~ 14	−0.2 ~ −4.7	167 ~ 219	194(20)	0.35 ~ 7.45	5.32(20)

Notes: $T_{m,ice}$ = final melting temperature of ice; T_h = total homogenization temperature; [1] The number in the parentheses denotes number of measurements; [2] Salinities were calculated from the equations of Bodnar (1993).
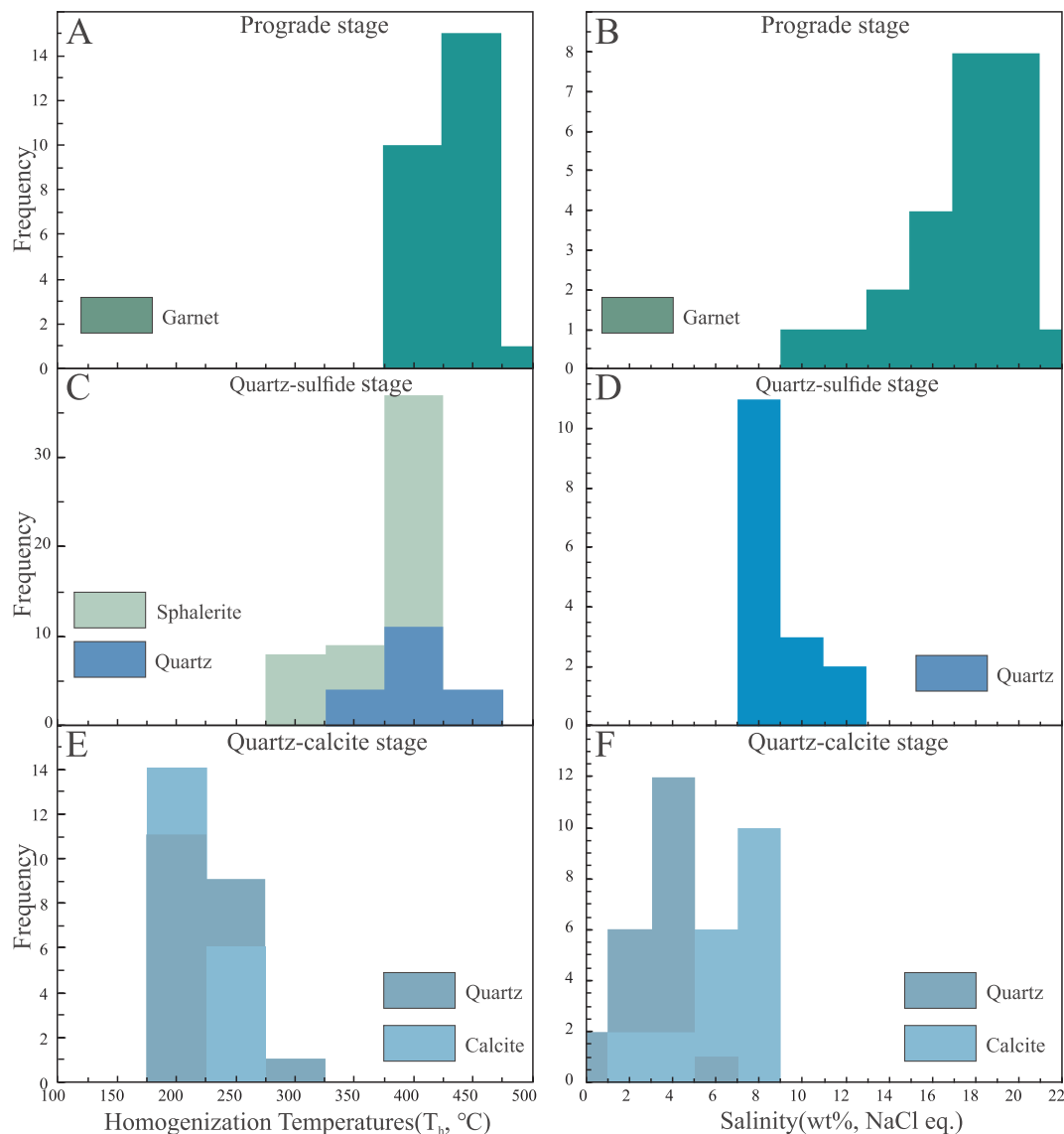
Fig. 9. Histograms of the total homogenization temperatures and salinities for fluid inclusions from the Tuboh deposit. The calculated temperature of the sphalerite is given in panel C.

Table 5
Sulfur Isotope Data of sulfides from the Tuboh Deposit.

Sample no.	Mineral	$\delta^{34}S_{V\text{-}CDT}$ (‰)
LM-2	Sphalerite	1.43
LM-04	Chalcopyrite	−1.09
	Galena	−2.44
LM-9	Sphalerite	1.63
LM-11	Sphalerite	−0.38
	Chalcopyrite	−0.46
	Galena	−2.00
LM-12	Sphalerite	1.66
	Galena	0.11
LM-13	Sphalerite	−0.18
	Galena	−1.74
LM-14	Galena	−0.12
LM-15	Sphalerite	2.52
	Galena	0.91
LM-16	Sphalerite	2.01
	Galena	0.36
LM-18	Sphalerite	−0.42
	Chalcopyrite	−0.44
	Galena	−2.26

quartz-sulfide stage (Fig. 9C). Moreover, the S fugacity for sphalerite crystallization is $10^{-9.7}$ to $10^{-7.1}$ bars, which is consistent with the range of S fugacity from pyrite–pyrrhotite–magnetite at 300–400 °C (log $fS_2 = -11.0$ to -7.2, Klshima, 1989). The S fugacity decreases with temperature reduction (Fig. 12). During the ore-forming process, the carbonaceous rock of the Rawas Formation could have been interacted with the ore-forming fluids. The reaction resulted in the activity of H^+ of ore-forming fluids decrease, and pH shift to neutral (So et al., 1993). Degassing of S was caused by cooling of the ore-forming fluids and opening of the ore system (Carroll and Webster, 1994; Palinkaš et al., 2013). Those were responsible for decreases in logfs_2. The pyrrhotite symbiosis with the chalcopyrite disease shown in the sphalerite indicates that S fugacity decreases in a local environment (Fig. 5E, F). Therefore, ore precipitation occurred in a progressive reducing environment (Fig. 12).

The homogenization temperatures of the garnet were 380–450 °C. Under high temperatures, wall rocks are ductile (Fournier, 1992) and seal mixtures of external fluids. Skarn can represent the physicochemical conditions of the prograde stage under a relatively closed environment. The fluid inclusions analysis covered all three ore-forming stages in this study, which revealed the complete hydrothermal history

Table 6
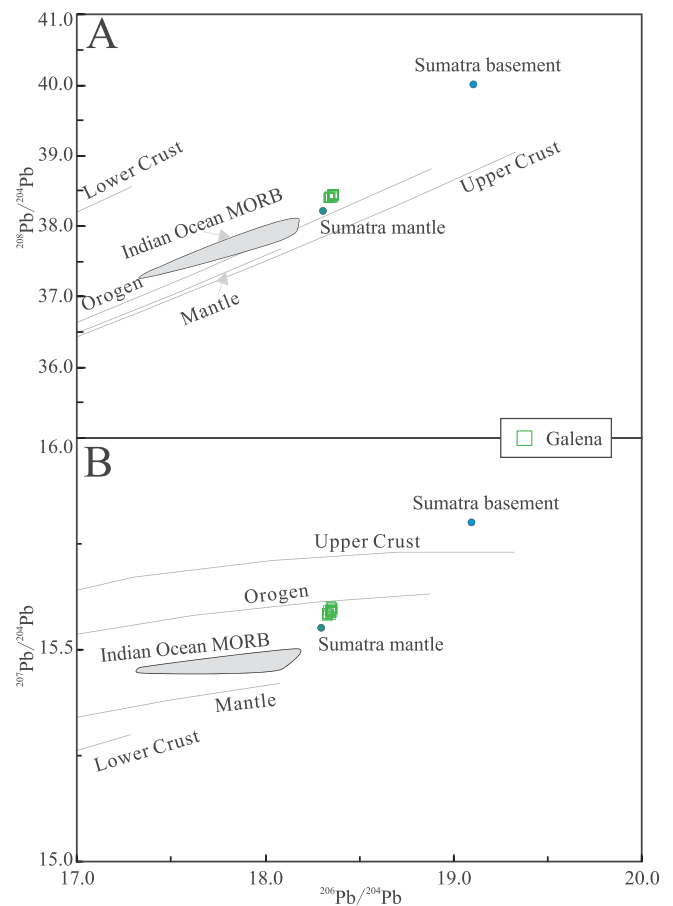Lead Isotopic Compositions of Galena from the Tuboh Deposit.

Sample No.	$^{208}Pb/^{204}Pb$	SE	$^{207}Pb/^{204}Pb$	SE	$^{206}Pb/^{204}Pb$	SE	$^{208}Pb/^{206}Pb$	SE	$^{207}Pb/^{206}Pb$	SE	$^{204}Hg/^{204}Pb$	SE
LM-11-1	38.402	0.004	15.589	0.001	18.359	0.001	2.0916	0.0001	0.8491	0.0000	0.000	0.000
LM-11-2	38.369	0.012	15.576	0.004	18.344	0.004	2.0915	0.0002	0.8491	0.0000	0.000	0.000
LM-11-3	38.378	0.011	15.580	0.004	18.347	0.004	2.0918	0.0002	0.8492	0.0000	0.000	0.000
LM-11-4	38.403	0.011	15.587	0.004	18.358	0.004	2.0917	0.0002	0.8490	0.0000	0.000	0.000
LM-11-5	38.424	0.007	15.597	0.003	18.369	0.003	2.0918	0.0001	0.8491	0.0000	0.000	0.000
LM-15-1	38.412	0.010	15.591	0.004	18.361	0.004	2.0920	0.0001	0.8492	0.0000	0.000	0.000
LM-15-2	38.405	0.006	15.589	0.002	18.360	0.002	2.0919	0.0001	0.8492	0.0000	0.000	0.000
LM-15-3	38.430	0.012	15.599	0.004	18.363	0.004	2.0928	0.0002	0.8495	0.0000	0.000	0.000
LM-04-1	38.396	0.007	15.590	0.003	18.348	0.003	2.0928	0.0001	0.8497	0.0000	0.000	0.000
LM-04-2	38.377	0.009	15.582	0.003	18.345	0.003	2.0920	0.0001	0.8495	0.0000	0.000	0.000
LM-04-3	38.379	0.010	15.583	0.004	18.344	0.004	2.0922	0.0001	0.8495	0.0000	0.000	0.000
LM-04-4	38.372	0.011	15.580	0.004	18.342	0.004	2.0920	0.0002	0.8495	0.0000	0.000	0.000
LM-04-5	38.397	0.012	15.588	0.004	18.361	0.004	2.0912	0.0002	0.8490	0.0000	0.000	0.000
LM-05-1	38.398	0.009	15.583	0.003	18.364	0.003	2.0906	0.0001	0.8486	0.0000	0.000	0.000
LM-05-2	38.380	0.004	15.580	0.001	18.361	0.001	2.0902	0.0000	0.8486	0.0000	0.000	0.000
LM-05-3	38.430	0.026	15.597	0.009	18.370	0.009	2.0918	0.0003	0.8490	0.0001	0.000	0.000
LM-05-4	38.400	0.020	15.587	0.007	18.360	0.007	2.0916	0.0003	0.8490	0.0001	0.000	0.000
LM-12-1	38.399	0.004	15.585	0.001	18.363	0.002	2.0912	0.0001	0.8488	0.0000	0.000	0.000
LM-12-2	38.400	0.004	15.585	0.002	18.362	0.002	2.0913	0.0000	0.8488	0.0000	0.000	0.000
LM-12-3	38.406	0.004	15.589	0.001	18.363	0.001	2.0915	0.0000	0.8489	0.0000	0.000	0.000
LM-12-4	38.411	0.006	15.590	0.002	18.364	0.002	2.0915	0.0001	0.8489	0.0000	0.000	0.000
LM-12-5	38.415	0.007	15.592	0.003	18.365	0.003	2.0917	0.0001	0.8490	0.0000	0.000	0.000
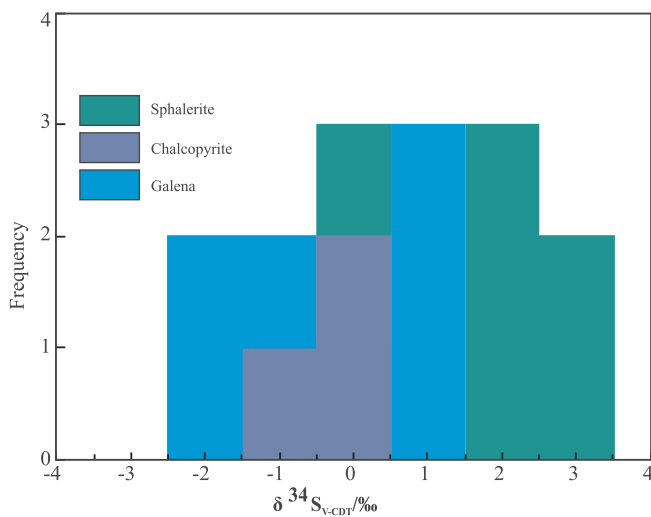
Fig. 10. Histogram of S isotopic compositions for sulfides of the Tuboh deposit.

Fig. 11. A. $^{208}Pb/^{204}Pb$ versus $^{206}Pb/^{204}Pb$ and (B.) $^{207}Pb/^{204}Pb$ versus $^{206}Pb/^{204}Pb$ plots for the Tuboh deposit (Zartman and Doe, 1981).

of the Tuboh deposit (Fig. 13).

The homogenization temperatures of fluid inclusions in garnet from prograde stage were 380 to 450 °C, and salinities were 9.21 to 21.4 wt% NaCl equivalent, which are consistent with magmatic hydrothermal fluids (Einaudi et al., 1981; Chen et al., 2007). The salinities of fluid inclusions in quartz from quartz-sulfide stage range between 6.45 and 11.1 wt% NaCl equivalent, which are agree with the salinity of magmatic derived fluids under hydrostatic pressures (6–8 wt% NaCl equivalent; Fournier, 1999; Baker et al., 2004). Thus, ore-forming fluid may be derived from magmatic fluids. The microthermometric data revealed that the ore-forming fluid ultimately evolved into 194 °C and 5.32 wt% NaCl equivalent in the quartz–calcite stage. This decreasing trend in the homogenization temperature coupled with calculated salinity clearly indicates the continuous addition of meteoric water into the magmatic ore-forming fluid (Wilkinson, 2001). Fluid mixing is considered to be the principal mechanism affecting mineral deposition in hydrothermal mineralization systems (e.g., Giuliani et al., 1993; Fusswinkel et al., 2013; Yang et al., 2015). Therefore, sulfide precipitation is a result of fluid mixing.

5.3. Occurrence of Ag

The EPMA analyses revealed that the Ag is mainly hosted by galena from the quartz-sulfide stage at 0.05–0.14 wt% (Table 4). The distribution of Ag in galena has been extensively studied as microinclusions of Ag-bearing minerals or as a solid-solution form (Craig, 1967;
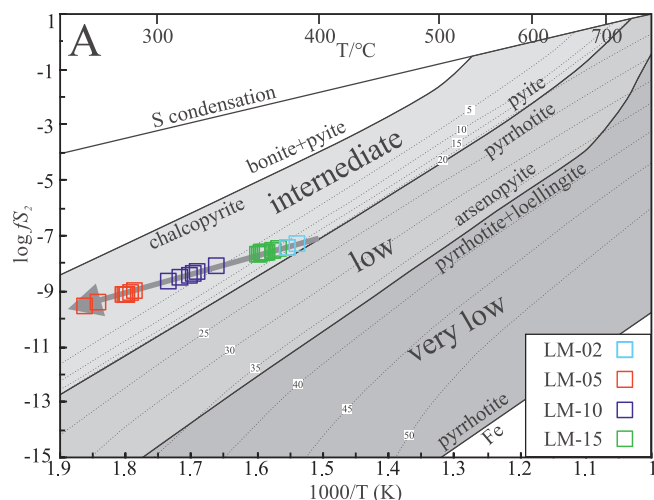
Fig. 12. Bivariate plot of log fS_2 versus sphalerite temperature (after Vaughan and Craig, 1997). The mole percent of FeS in the sphalerite was collected from Scott and Barnes (1971); the sulfidation states were adapted from Einaudi et al. (2003); and the sulfide stabilities are cited from Barton and Skinner (1979).
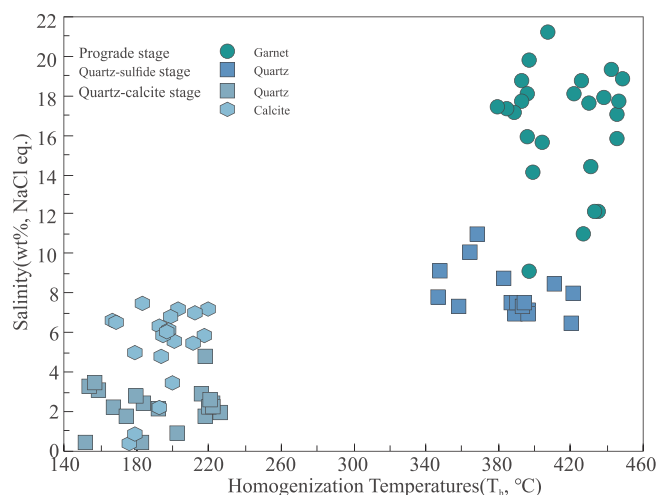
Fig. 13. Total homogenization temperature versus salinity diagram for fluid inclusions of the Tuboh deposit.

Amcoff, 1984; Zeng et al., 2000, and references therein; Bonev, 2007; Chutas et al., 2008; Renock and Becker, 2011; George et al., 2015; Grant et al., 2015).

Optical microscopy, scanning electron microscopy (SEM) and EPMA results illustrated that independent Ag minerals are free in the Tuboh deposit. The EPMA analysis also showed that the galena is rich in Ag, and galena grains have homogeneous Ag with no oscillated zone or abnormal enrichment points or areas (Fig. 14B). This confirms that the Ag is present as a lattice-bound substitution rather than microinclusions in the galena. The EPMA mapping feature of Bi is similar to that of Ag and Pb (Fig. 14C, D), demonstrating that the Ag occurs as $PbS–AgBiS_2$ solid solution in the galena.

The Ag and Bi have a significant positive correlation ($R^2 = 0.95$) and obviously negative correlation with Pb ($R^2 = 0.80$; Fig. 14E, F). These linear relationships indicate that Ag occurs as solid solution in galena by a coupled substitution mechanism involving $Ag^+ + Bi^{3+} = 2Pb^{2+}$, which occupies two Pb^{2+} ions of octahedral sites (Foord et al., 1988; Costagliola et al., 2003). The presence of Bi^{3+} promoted significant quantities of Ag to form in the galena (Chutas et al., 2008; Renock and Becker, 2011). Massive galena precipitates at 270–420 °C from the prograde stage, where the solid solution of

$PbS–AgBiS_2$ is incomplete (Amcoff, 1976). Thus, the Ag replaced the Pb by coupled substitution with Bi and occurs as invisible Ag via $PbS–AgBiS_2$ solid solution in the galena.

5.4. Metallogenic type

The Tuboh deposit is situated at the contact between the Woyla Nappe and the Sundaland Arc and is related to the Sumatra fault system (Wajzer et al., 1991; McCarthy, 1997). This deposit is also controlled by arc magmatism of the Barisan Range (Curray et al., 1979; Curray, 1989; McCarthy and Elders, 1997). The geological investigations indicate that the mineralization is close to skarn and is the result of Eocene Jangkat quartz monzonite intrusion into the limestone of the Rawas Formation. Thus, the metallogenic age is Eocene. The orebodies mainly occurred within the contact zone between the intrusion and marble, and were mainly hosted by marble and hornfels within the Rawas Formation, that suffered skarnization, chloritization, silicification, and carbonation alteration. The mineralization processes are consistent with the major stages of skarn-type deposits, including the prograde stage, retrograde stage, ore quartz-sulfide stage and post-ore quartz-calcite stage. Therefore, the Tuboh deposit is a skarn-type deposit. The ore minerals are dominant by sphalerite and galena with minor pyrite and chalcopyrite in the Tuboh deposit. And the composition of garnet is similar to that in the Zn-type skarn deposits (Fig. 15; Meinert et al., 2005).

As previously mentioned, the series of intrusions is widespread in the Jangkat ore field and is associated with skarn Au–Fe mineralization (Fig. 2; JICA, 1987; Prayogo, 2009). The Muaramangkulan quartz diorite (83.6 ± 4.2 Ma) is close to skarn-type Au mineralization, and the Raja granite (54.1 ± 2.7 Ma) and the Pulaukidak quartz monzonite (51.9 ± 2.7 Ma) are related to skarn-type Fe mineralization. These intrusions are different in age, indicating that Late Cretaceous and Eocene magmatism and metallogenesis occurred in the ore field. Thus, further research is needed to better understand the genetic relationship of skarn mineralization and magmatism, which have great significance for revealing the tectonic–magmatic–metallogenic system in the Sundaland Arc.
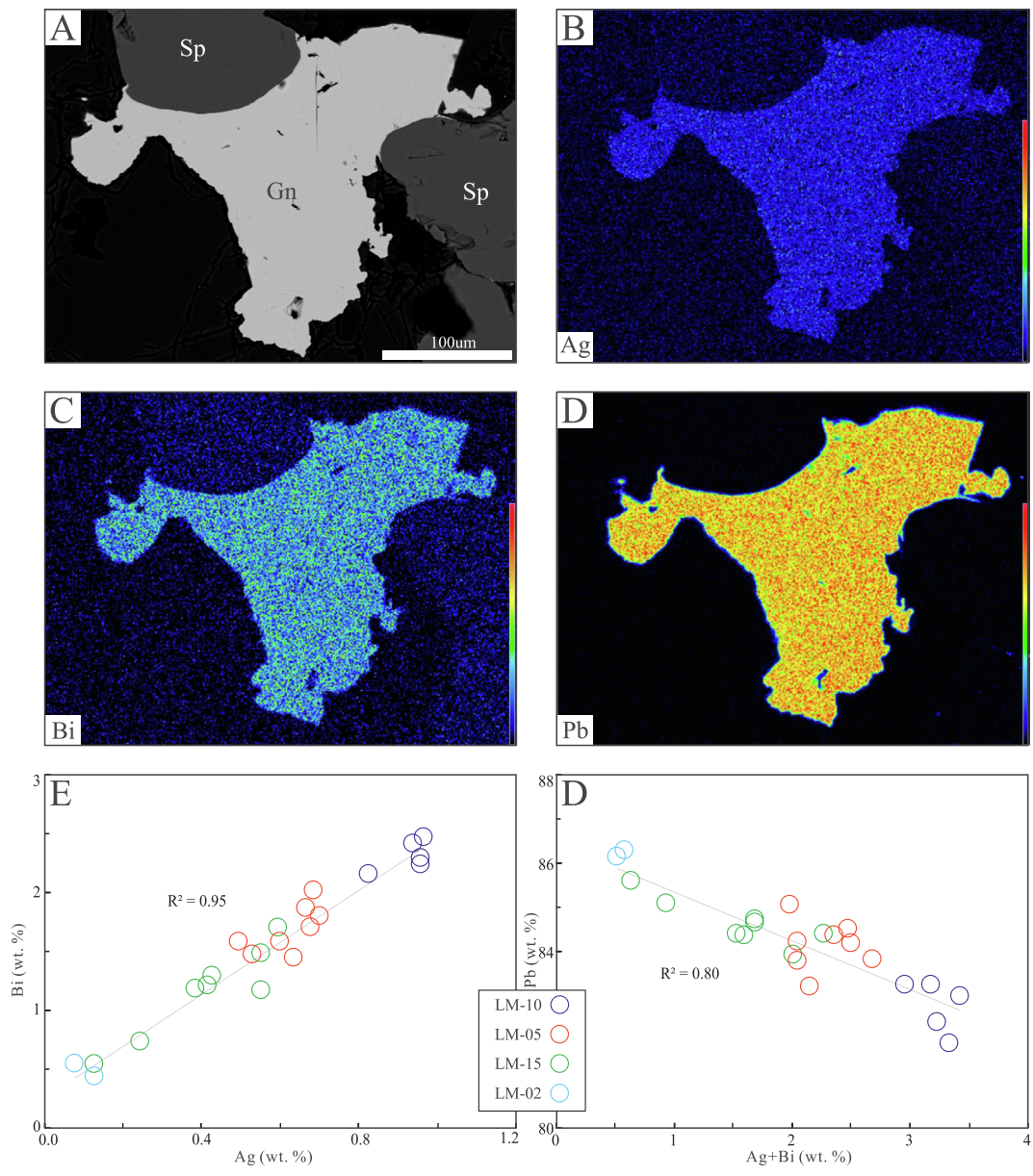
6. Conclusions

The important conclusions from this study can be summarized as follows:

(1) S-Pb isotopes of sulfides and fluid inclusions data indicate that the ore-forming components were mainly derived from the Eocene Jangkat quartz monzonite.
(2) Garnet is rich in andradite, which suggests the skarn was formed under relatively oxidized conditions. Decreases of temperature and logfS_2, and fluid mixing of the ore-forming fluid were likely the key triggers for ore precipitation.
(3) Mineralogical and textural evidence indicate that Ag is primarily hosted by galena as solid solution and Pb is replaced by Ag + Bi via coupled substitution.
(4) The Tuboh deposit is a skarn-type Pb–Zn–Ag polymetallic deposit.

Fig. 14. A. Reflected light image and (B.–D.) EPMA element mapping of a galena grain; (E.) bivariate plot of Bi versus Ag; and (F.) bivariate plot of Pb versus Ag + Bi in galena of the Tuboh deposit.
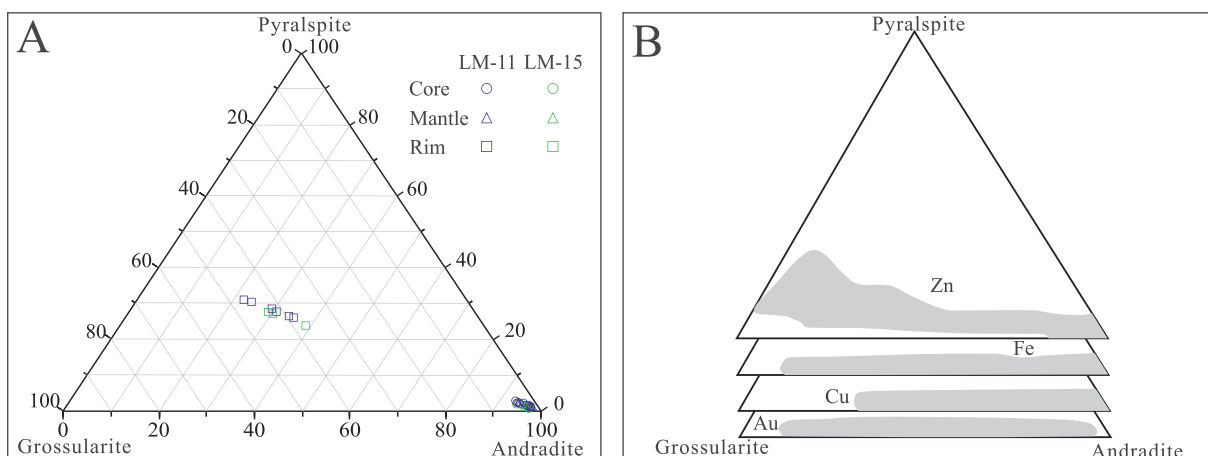
Fig. 15. A. Ternary plots of garnet compositions from the Tuboh deposit; (B.) garnet-related skarn-type deposits (data from Meinert et al., 2005).

References

Abidin, H.Z., 2010. Characteristics of the Arai Granite associated with the iron ore and Zn-Cu-Pb deposits in Musi Rawas Regency, south Sumatera. Jurnal Geologi dan Sumberdaya Mineral 20 (3), 133–146.

Abidin, H.Z., Utoyo, H., 2014. Mineralization of the selected base metal deposits in the Barisan Range, Sumatera, Indonesia (case study at Lokop, Dairi, Latong, Tanjung Balit and Tubah). Indonesian Mining J. 17 (3), 122–133.

Amcoff, Ö., 1976. The solubility of silver and antimony in galena. Neues Jahrbuch für Mineralogie Monatshefte 6, 247–261.

Amcoff, Ö., 1984. Distribution of silver in massive sulfide ores. Miner. Deposita 19 (1), 63–69.

Baker, T., Achterberg, E.V., Ryan, C.G., Lang, J.R., 2004. Composition and evolution of ore fluids in a magmatic-hydrothermal skarn deposit. Geology 32, 117–120.

Bao, Z., Chen, L., Zong, C., Yuan, H., Chen, K., Dai, M., 2017. Development of pressed sulfide powder tablets for in situ sulfur and lead isotope measurement using LA-MC-ICP-MS. Int. J. Mass Spectrom. 421, 255–262.

Barber, A.J., 2000. The origin of the Woyla Terranes in Sumatra and the Late Mesozoic evolution of the Sundaland margin. J. Asian Earth Sci. 18 (6), 713–738.

Barber, A.J., Crow, M.J., 2003. An evaluation of plate tectonic models for the development of Sumatra. Gondwana Res. 6, 1–28.

Barber, A.J., Crow, M.J., 2005. Pre-tertiary stratigraphy. In: Barber, A.J., Crow, M.J., Milsom, J.S. (Eds.), Sumatra: Geology, Resources and Tectonic Evolution. Geological Society, London, Memoirs, pp. 24–53 31(1).

Barton Jr, P.B., Skinner, B.J., 1979. Sulfide mineral stabilities. In: Barnes, H.L. (Ed.), Geochemistry of Hydrothermal Ore Deposits, 2nd. Holt and Wiley, New York, pp. 278–403.

Beddoe-stephens, B., Shepherd, T.J., Bowles, J.F.W., Brook, M., 1987. Gold mineralization and skarn Development near Muara Sipongi, West Sumatra, Indonesia. Econ. Geol. 82, 1732–1749.

Bodnar, R.J., 1993. Revised equation and table for determining the freezing point depression of H_2O-NaCl solutions. Geochim. Cosmochim. Acta 57 (3), 683–684.

Bonev, I.K., 2007. Crystal habit of Ag-, Sb-and Bi-bearing galena from the Pb-Zn ore deposits in the Rhodope Mountains. Geochem., Mineral. Petrol. 45, 1–18.

Bonsall, T.A., Spry, P.G., Voudouris, P.C., Tombros, S., Seymour, K.S., Melfos, V., 2011. The geochemistry of carbonate-replacement Pb-Zn-Ag mineralization in the Lavrion district, Attica, Greece: fluid inclusion, stable isotope, and rare earth element studies. Econ. Geol. 106 (4), 619–651.

Cameron, N.R., Clarke, M.C.G., Aldiss, D.T., Aspden, J.A., Djunuddin, A., 1980. The geological evolution of northern Sumatra. Jakarta In: Indonesian Petroleum Association, Proceedings 9th Annual Convention, pp. 149–187.

Carr, G.R., Dean, J.A., Suppel, D.W., Heithersay, P.S., 1995. Precise lead isotope fingerprinting of hydrothermal activity associated with Ordovician to Carboniferous metallogenic events in the Lachlan fold belt of New South Wales. Econ. Geol. 90 (6), 1467–1505.

Carroll, M.R., Webster, J.D., 1994. Solubilities of sulfur, noble gases, nitrogen, chlorine, and fluorine in magmas. Rev. Mineral. Geochem. 30, 231–279.

Chen, Y.J., Chen, H.Y., Zaw, K., Pirajno, F., Zhang, Z.J., 2007. Geodynamic settings and tectonic model of skarn gold deposits in China: an overview. Ore Geol. Rev. 31, 139–169.

Chen, K.Y., Yuan, H.L., Bao, Z.A., Zong, C.L., Dai, M.N., 2014. Precise and accurate in situ determination of lead isotope ratios in NIST, USGS, MPI-DING and CGSG glass reference materials using femtosecond laser ablation MC-ICP-MS. Geostand. Geoanal. Res. 38 (1), 5–21.

Chutas, N.I., Kress, V.C., Ghiorso, M.S., Sack, R.O., 2008. A solution model for high-temperature PbS-AgSbS2-AgBiS2 galena. Am. Mineral. 93 (10), 1630–1640.

Clake, M.C.G., Beddoe-stephens, B., 1987. Geochemistry, mineralogy and plate-tectonic setting of a Late Cretaceous Sn-W Granite from Sumatra, Indonesia. Mineral. Mag. 51, 371–387.

Cobbing, E.J., 2005. Granites. In: Barber, A.J., Crow, M.J., Milsom, J.S. (Eds.), Sumatra: Geology, Resources and Tectonic Evolution. Geological Society, London, Memoirs, pp. 54–62 31(1).

Costagliola, P., Di Venedetto, F., Benvenuti, M., Bernardini, G.P., Cipriani, C., Lattanzi, P.F., Romanelli, M., 2003. Chemical speciation of Ag in galena by EPR spectroscopy. Am. Mineral. 88, 1345–1350.

Craig, J.R., 1967. Phase relations and mineral assemblages in the Ag-Bi-Pb-S system. Miner. Deposita 1 (4), 278–306.

Curray, J.R., 1989. The Sunda Arc: a model for oblique plate convergence. Neth. J. Sea Res. 24 (2–3), 131–140.

Curray, J.R., Moore, D.G., Lawver, L.A., Emmel, F.J., Raitt, R.W., Henry, M., Kieckhefer, R., 1979. Tectonics of the Andaman Sea and Burma. In: Watkins, J.S., Montadert, L., Dickenson, P.W. (Eds.), Geological and Geophysical Investigations of Continental Margins. American Association of Petroleum Geologists, Memoirs, pp. 189–198.

Darbyshire, D.P.E., 1988. South-East Asia granite project-geochronology of tin islands granites, Indonesia: Natural Environment Research Council Isotope Geology Centre (London), Report No. 88(4), 32.

Einaudi, M.T., Meinert, L.D., Newberry, R.J., 1981. Skarn deposits. Econ. Geol. 75, 317–391.

Einaudi, M.T., Hedenquist, J.W., Inan, E.E., 2003. Sulfidation state of fluids in active and extinct hydrothermal systems: transitions from porphyry to epithermal environments. Spec. Public.-Soc. Econ. Geol. 10, 285–314.

Foord, E.E., Shawe, D.R., Conklin, N.M., 1988. Coexisting galena, PbS and sulfosalts: evidence for multiple episodes of mineralization in the Round Mountain and Manhattan Gold Districts, Nevada. Can. Mineral. 26, 355–376.

Fournier, R.O., 1992. The influences of depth of burial and the brittle-plastic transition on the evolution of magmatic fluids. Geol. Survey Japan Rep. 279, 57–59.

Fournier, R.O., 1999. Hydrothermal processes related to movement of fluid from plastic into brittle rock in the magmatic-epithermal environment. Econ. Geol. 94 (8), 1193–1211.

Fusswinkel, T., Wagner, T., Walle, M., Wenzel, T., Heinrich, C.A., Markl, G., 2013. Fluid mixing forms basement-hosted Pb-Zn deposits: insight from metal and halogen geochemistry of individual fluid inclusions. Geology 41 (6), 679–682.

Garwin, S., Hall, R., Watanabe, Y., 2005. Supplement to: tectonic setting, geology, and gold and coppermineralisation in Cenozoic magmatic arcs of Southeast Asia and the West Pacific. In: Economic Geology 100th Anniversary Volume, pp. 891–930.

Gasparon, M., Varne, R., 1998. Crustal assimilation versus subducted sediment input in west Sunda arc volcanics an evaluation. Miner. Petrol. 64 (1–4), 89–117.

George, L., Cook, N.J., Ciobanu, C.L., Wade, B.P., 2015. Trace and minor elements in galena A reconnaissance LA-ICP-MS study. Am. Mineral. 100 (2–3), 548–569.

Giuliani, G., Olivo, G.R., Marini, O.J., Michel, D., 1993. The Santa rita gold deposit in the proterozoic Paranoa group, Goias, Brazil: an example of fluid mixing during ore deposition. Ore Geol. Rev. 8 (6), 503–523.

Grant, H.L., Layton-Matthews, D., Peter, J.M., 2015. Distribution and controls on silver mineralization in the Hackett River Main Zone, Nunavut, Canada: an Ag-and Pb-enriched Archean volcanogenic massive sulfide deposit. Econ. Geol. 110 (4), 943–982.

Hall, R., 1996. Reconstructing SE Asia. In: Hall, R., Blundell, D. (Eds.), Tectonic Evolution of Southeast Asia. Geological Society, London, Special Publications, pp. 153–184.

Hall, R., 2002. Cenozoic geological and plate tectonic evolution of SE Asia and the SW Pacific: computer-based reconstructions, model and animations. J. Asian Earth Sci. 20, 353–431.

Hamilton, W.B., 1979. Tectonics of the Indonesian region. United States Geological Survey Professional Paper, p. 345.

Herzig, P.M., 1988. A mineralogical, geochemical and thermal profile trough the Agrokipia "B" hydrothermal sulfide deposit, Troodos Ophiolite Complex, Cyprus. In: Friedrich, G.H., Herzig, P.M. (Eds.), Base Metal Sulfide Deposits. Springer-Verlag, Berlin, Heidelberg, pp. 182–215.

Hu, P., Zhu, Z., Xiang, W., 2014. The Lithogeochemical Characteristics and Tectonic Setting Research of Sulit Skarn-Type Copper Deposit in Sumatra Island, Indonesia. Acta Geol. Sin. (English Edition) 88 (s2) 875-875.

Hutchison, C.S., 1994. Gondwana and Cathaysian blocks, Palaeotethys sutures and Cenozoic tectonics in South-east Asia Active Continental Margins-Present and Past. Springer, Berlin, Heidelberg, pp. 388–405.

Imtihanah,, 2000. Isotopic Dating of Igneous Sequences of the Sumatra Fault System. Master thesis. London University, pp. 150.

Ito, E., White, W.M., Göpel, C., 1987. The O, Sr, Nd and Pb isotope geochemistry of MORB. Chem. Geol. 62 (3–4), 157–176.

JICA, 1986. Report on the cooperative mineral exploration of southern Sumatra: Phase 1. (unpublished Report). p. 167.

JICA, 1987. Report on the cooperative mineral exploration of southern Sumatra: Phase 2. (unpublished Report). p. 216.

JICA, 1988. Report on the cooperative mineral exploration of southern Sumatra: Phase 3. (unpublished Report). p. 194.

Jobson, D.H., Boulter, C.A., Foster, R.P., 1994. Structural controls and genesis of epithermal gold-bearing breccias at the Lebong Tandai mine, Western Sumatra, Indonesia. J. Geochem. Exploration 50 (1–3), 409–428.

Kajiwara, Y., Krouse, H.R., 1971. Sulfur isotope partitioning in metallic sulfide systems. Can. J. Earth Sci. 8, 1397–1408.

Katili, J.A., 1973. Geochronology of west Indonesia and its implication on plate tectonics. Tectonophysics 19, 195–212.

Keith, M., Haase, K.M., Schwarz-Schampera, U., Klemd, R., Petersen, S., Bach, W., 2014. Effects of temperature, sulfur, and oxygen fugacity on the composition of sphalerite from submarine hydrothermal vents. Geology 42 (8), 699–702.

Klshima, N., 1989. A thermodynamic study on the pyrite-pyrrhotite-magnetite-water system at 300–500° C with relevance to the fugacity/concentration quotient of aqueous H_2S. Geochim. Cosmochim. Acta 53 (9), 2143–2155.

Kwak, T.A.P., 1987. W-Sn skarn deposits and related metamorphic skarns and granitoids. In: Developments in Economic Geology 24. Elsevier, Amsterdam, The Netherlands, pp. 82–84.

Maryono, A., Natawidjaja, D.H., van Leeuwen, T.M., Harrison, R.L., Santoso, B., 2014. Sumatra, an emerging world-class magmatic gold belt. In: Proceedings of Sundaland Resources, 2014 Mgei Annual Convention, pp. 89–101.

McCarthy, A.J., 1997. The evolution of the transcurrent Sumatran Fault System. PhD Thesis. University of London, pp. 231.

McCarthy, A.J., Elders, C.F., 1997. Cenozoic deformation in Sumatra: oblique subduction and the development of the Sumatran Fault System. In: Fraser, A.J., Matthews, S.J. (Eds.), Petroleum Geology of Southeast Asia. Geological Society, London, Special Publications, pp. 355–363 126(1).

McCourt, W.J., Crow, M.J., Cobbing, E.J., Amin, T.C., 1996. Mesozoic and Cenozoic plutonic evolution of SE Asia: evidence from Sumatra, Indonesia. In: Hall, R., Blundell, D.J. (Eds.), Tectonic Evolution of Southeast Asia. Geological Society, London, Special Publications, pp. 321–335.

Meinert, L.D., Diple, G.M., Nicolescu, S., 2005. World skarn deposits. In: Economic Geology 100th Anniversary Volume. Society of Economic Geologist, Inc., pp. 299–336.

Metcalfe, I., 1996. Gondwanaland dispersion, Asian accretion and evolution of Eastern Tethys. Aust. J. Earth Sci. 43 (6), 605–623.

Metcalfe, I., 2006. Palaeozoic and Mesozoic tectonic evolution and palaeogeography of East Asian crustal fragments: the Korean Peninsula in context. Gondwana Res. 9, 24–46.

Metcalfe, I., 2011. Tectonic framework and Phanerozoic evolution of Sundaland.

Gondwana Res. 19 (1), 3–21.

Newberry, R.J., 1983. The formation of subcalcic garnet in scheelite-bearing skarns. Can. Mineral. 21, 529–544.

Ng, S.W.P., Whitehouse, M.J., Roselee, M.H., Teschner, C., Murtadha, S., Oliver, G.J., Ghani, A.A., Chang, S.C., 2017. Late Triassic granites from Bangka, Indonesia: a continuation of the Main Range granite province of the South-East Asian Tin Belt. J. Asian Earth Sci. 138, 548–561.

Ohmoto, H., 1986. Stable isotope geochemistry of ore deposits. Rev. Mineral. Geochem. 16 (1), 491–559.

Ohmoto, H., Rye, R.O., 1979. Isotopes of sulfur and carbon. In: Barnes, H.L. (Ed.), Geochemistry of Hydrothermal Ore Deposits, 2nd. Wiley, New York, pp. 509–567.

Palinkaš, S.S., Palinkaš, L.A., Renac, C., Spangenberg, J.E., Lüders, V., Molnar, F., Maliqi, G., 2013. Metallogenic model of the Trepča Pb-Zn-Ag skarn deposit, Kosovo: evidence from fluid inclusions, rare earth elements, and stable isotope data. Econ. Geol. 108 (1), 135–162.

Prayogo, 2009. Geological report of the Tuboh prospect. PT. Galtam Indonesia. (unpublished Report). p. 43.

Pulunggono, A., Cameron, N.R., 1984. Sumatran microplates, their characteristics and their role in the evolution of the Central and South Sumatra basins. In: Proceedings of the 13th Annual Convention. Indonesian Petroleum Association, pp. 1221–1443.

Renock, D., Becker, U., 2011. A first principles study of coupled substitution in galena. Ore Geol. Rev. 42 (1), 71–83.

Ripley, E.M., 1986. Application of Stable Isotopic Studies to Problems of Magmatic Sulfide Ore Genesis with Special Reference to the Duluth Complex, Minnesota. Geology and Metallogeny of Copper Deposits. Springer, Berlin, Heidelberg, pp. 25–42.

Saing, S., Takahashi, R., Imai, A., 2015. Fluid inclusion and stable isotope study at the southeastern Martabe Deposit: Purnama, Barani and Horas Ore Bodies, North Sumatra, Indonesia. Resour. Geol. 66 (2), 127–148.

Schwartz, M.O., Surjono,, 1990a. Greisenization and albitization at the Tikus tin-tungsten deposit, Belitung, Indonesia. Econ. Geol. 85, 691–713.

Schwartz, M.O., Surjono,, 1990b. The strata-bound Tin deposit Nam Salu, Kelapa Kampit, Indonesia. Econ. Geol. 85, 76–98.

Schwartz, M.O., Surjono,, 1991. The pemali tin deposit, Bangka, Indonesia. Miner. Deposita 26, 18–25.

Scott, S.D., Barnes, H.L., 1971. Sphalerite geothermometry and geobarometry. Econ. Geol. 66 (4), 653–669.

Şengör, A.M.C., 1984. The Cimmeride orogenic system and the tectonics of Eurasia. Geological Society of America, Special Papers, 195, 1–74.

So, C.S., Yun, S.T., Koh, Y.K., 1993. Mineralogic, fluid inclusion, and stable isotope evidence for the genesis of carbonate-hosted Pb-Zn (-Ag) orebodies of the Taebaek Deposit, Republic of Korea. Econ. Geol. 88 (4), 855–872.

Susanto, A., Suparka, E., 2012. Hydrothermal alteration and mineralization of porphyry-skarn deposits in the Geunteut area, Nanggroe Aceh Darussalam, Indonesia. Bull. Geol. Soc. Malaysia 58, 15–21.

Sutopo, B., 2011. The Martabe Au-Ag High Sulfidation Epithermal deposits, Sumatra: Implications for Ore Genesis and Exploration. University of Tasmania, pp. 352 Ph D Thesis.

Suwarna, N., Santosa, S., Koesoemadinata, S., 1989. Geological Map of the Ende Quadrangle, East NusaTenggara, scale 1:250 000. Geological Research and Development Centre, Bandung.

van Leeuwen, T.M., Taylor, R.P., Hutagalung, J., 1987. The geology of the Tangse porphyry copper-molybdenum prospect, Aceh, Indonesia. Econ. Geol. 82 (1), 27–42.

Vaughan, D.J., Craig, J.R., 1997. Sulfide ore mineral stabilities, morphologies, and intergrowth textures. In: Barnes, H.L. (Ed.), Geochemistry of Hydrothermal Ore Deposits, 3rd ed. John Wiley, New York, pp. 367–434.

Wajzer, M.R., Barber, A.J., Hidayat, S., 1991. Accretion, collision and strike-slip faulting: the Woyla group as a key to the tectonic evolution of north Sumatra. J. Asian Earth Sci. 6 (3–4), 447–461.

Wheeler, R.S., Browne, P.R.L., Rodgers, A.K., 2001. Iron-rich and iron-poor prehnites from the Way Linggo epithermal Au-Ag deposit, southwest Sumatra, and the Heber geothermal field, California. Mineral. Mag. 65 (3), 397–406.

Wilkinson, J.J., 2001. Fluid inclusions in hydrothermal ore deposits. Lithos 55, 229–272.

Williamson, A., Fleming, G.J., 1995. Miwah prospect high sulphidation Au-Cu mineralisation, northern Sumatra, Indonesia. In: PACRIM, '95. Australian Institute of Mining and Metallurgy, pp. 637–642.

Yang, L., Wang, Q., Liu, X., 2015. Correlation between mineralization intensity and fluid-rock reaction in the Xinli gold deposit, Jiaodong peninsula, China: constraints from petrographic and statistical approaches. Ore Geol. Rev. 71, 29–39.

Yuan, H.L., Yin, C., Liu, X., Chen, K.Y., Bao, Z.A., Zong, C.L., 2015. High precision in-situ, pb isotopic analysis of sulfide minerals by femtosecond laser ablation multi-collector inductively coupled plasma mass spectrometry. Sci. China Earth Sci. 58 (10), 1713–1721.

Zartman, R.E., Doe, B.R., 1981. Plumbotectonics-the model. Tectonophysics 75 (1–2), 135–162.

Zeng, N., Izawa, E., Motomura, Y., Lai, L., 2000. Silver minerals and paragenesis in the Kangjiawan Pb–Zn–Ag–Au deposit of the Shuikoushan mineral district, Hunan Province, China. Can. Mineral. 38 (1), 11–22.

Zhou, J., Huang, Z., Zhou, M., Li, X., Jin, Z., 2013. Constraints of C–O–S–Pb isotope compositions and Rb–Sr isotopic age on the origin of the Tianqiao carbonate-hosted Pb–Zn deposit, SW China. Ore Geol. Rev. 53, 77–92.